

1 **Revealing Hidden Oxygen Variability in the North Pacific: A Two-**
2 **Decade Analysis Using GOBAI-O₂**

3
4

5 Miho Ishizu^{1,2}, Tomomichi Ogata³

6

7 *¹Center for Climate Physics, Institute for Basic Science, Busan 46241, Republic of Korea*

8 *²Pusan National University, Tonghapgigyegwan Bldg 2 Busandaehak-ro, 63 beon-gil, Geumjeong-gu,*
9 *Busan 46241, Republic of Korea*

10 *³Japan Agency for Marine-Earth Science and Technology, Environmental Variability Prediction and*
11 *Application Research Group, Yokohama Institute for Earth Sciences, 3173-25 Showa-machi,*
12 *Kanagawa-ku, Yokohama 236-0001, Japan*

13 To whom correspondence may be addressed. Email: mishizu@pusan.ac.kr

14

15

16 **Abstract**

17 Oceanic dissolved oxygen concentrations are thought to be declining under ongoing global warming,
18 yet their variability remains less well understood than that of physical parameters such as temperature
19 and salinity, primarily due to the limited spatial and temporal coverage of oxygen observation. Here,
20 we examine linear trends in potential temperature, salinity, and dissolved oxygen in the North Pacific
21 over the past two decades (2004–2023), using the GOBAI-O₂ dataset (Version 4.4). We compare the
22 diagnosed oxygen trends with those of physical parameters to reveal the spatial structure of recent
23 changes. The oxygen trends inferred from GOBAI-O₂ are broadly consistent with trends observed
24 along ship-based hydrographic repeat lines. While basin-scale deoxygenation is evident, we also
25 identify localized oxygen increases on specific density surfaces. By relating these patterns to the

26 surrounding physical environment, we find that the spatial heterogeneity in oxygen trends is consistent
27 with known oceanographic processes, including the southward retreat of the oxygen minimum layer
28 and the northward migration of a front separating the subtropical and subarctic gyres. These results
29 underscore the value of GOBAI-O₂ data in linking physical variability to previously unrecognized
30 biological and biogeochemical patterns in the ocean.

31

32

33 **Plain Language Summary**

34 1. We investigated how potential temperature, salinity, and dissolved oxygen have changed in the
35 North Pacific over the past 20 years using GOBAI-O₂ dataset (Version 4.4), and we examined the
36 physical processes responsible for these trends.

37 2. The trends identified in this study are broadly consistent with findings from previous research, and
38 improved spatial coverage of GOBAI-O₂ allowed us to reveal connections between regional
39 patterns that we previously only partially understood.

40 3. Overall, dissolved oxygen decreased across much of the North Pacific. However, some regions
41 showed increasing oxygen levels, indicating that the changes were not uniform. These non-uniform
42 patterns reflect known physical ocean processes. For example, higher oxygen levels in the northern
43 North Pacific are consistent with a northward shift of the front separating the subtropical and
44 subarctic gyres. In the equatorial Pacific, the reduced westward extent of the oxygen minimum
45 layer corresponds to a weakening and poleward shift of the North Equatorial Countercurrent
46 (NECC) on interdecadal timescales.

47 4. These findings provide new evidence that links large-scale physical ocean changes to previously
48 unclear changes in biological and biogeochemical observations.

49

50 Keywords: dissolved oxygen, 20-year linear trends, Bio-Argo float data, global warming

51

52 **1. Introduction**

53 Over recent decades, the global ocean has experienced a decline in its dissolved oxygen inventory, a
54 trend projected to continue through the 21st century [Keeling et al., 2010; Breitburg et al., 2018;
55 Stramma and Schmidtko, 2021; Limburg et al., 2020; Ito et al., 2017, 2024; Kolodziejczyk et al., 2024].
56 This deoxygenation is driven in part by reduced ocean oxygen solubility under rising sea-surface
57 temperatures, which promotes oxygen outgassing. In addition, enhanced stratification and a slowdown
58 of ocean circulation under global warming can reduce interior ventilation and oxygen supply [Keeling
59 et al., 2010; Bopp et al. 2013; Ito et al. 2017]. Ocean oxygen loss can negatively affect aerobic marine
60 organisms [Pörtner and Farrell, 2008; Sampaio et al., 2021], alter biogeochemical cycles, and
61 potentially induce climate-relevant feedback [Berman-Frank et al., 2008]. Historical deoxygenation
62 has been inferred from globally distributed observations [Helm et al., 2011; Schmidtko et al., 2017;
63 Ito et al., 2017; Takatani et al., 2012; Sasano et al., 2015; Lauvset et al., 2022b], and Earth system
64 models have been used to simulate both historical and future changes in ocean oxygen [Bopp et al.,
65 2013; Kwiatkowski et al., 2020; Li et al. 2020].

66

67 Observed oxygen trends have traditionally been assessed using the discrete measurements of dissolved
68 oxygen concentration (O_2), typically obtained by Winkler titration [Winkler, 1988]. These
69 measurements are also used to calibrate electrode- and, more recently, optode-based oxygen sensors
70 mounted on conductivity-temperature-depth (CTD) profilers [Helm et al. 2011; Schmidtko et al.,
71 2017; Lauvset et al., 2022b]. Although programs such as WOCE, CLIVAR, and GO-SHIP have
72 collected high-quality oxygen measurements globally, repeat occupation intervals are commonly on
73 the order of a decade, limiting the ability to robustly quantify annual to seasonal variability. Higher-

74 frequency ship-based observations exist in a few regions [Takatani et al. 2012; Sasano et al., 2015],
75 but their spatial coverage is limited. Consequently, despite attempts to characterize basin-scale patterns
76 [Ito et al. 2017; Stramma et al. 2020; Kolodziejczyk et al. 2024], observational constraints have
77 hampered a spatially and temporally comprehensive understanding of dissolved oxygen variability and
78 trends.

79

80 Oxygen sensors were first deployed on Argo profiling floats in the mid-2000s. Since then,
81 approximately 1,800 oxygen-equipped floats have been deployed worldwide, substantially advancing
82 the observational basis for assessing oxygen variability and trends [Sharp et al., 2023]. The expansion
83 toward a global biogeochemical (BGC) Argo network has improved sampling in regions that were
84 previously sparsely observed [Claustre et al., 2020]. In parallel, major progress has been made in
85 calibration, adjustments, and quality control of oxygen measurements, including pre-deployment drift
86 corrections [D'Asaro and McNeil, 2013; Johnson et al., 2015; Bittig and Körtzinger, 2015; Bushinsky
87 et al., 2016; Drucker and Riser, 2016; Nicholson and Feen, 2017], climatology-based calibrations
88 [Takeshita et al., 2013], in-air oxygen measurement calibrations [Körtzinger et al., 2005; Bittig and
89 Körtzinger, 2015; Johnson et al., 2015; Bushinsky et al., 2016], post-deployment drift corrections
90 [Johnson et al., 2017; Bittig et al., 2018a, b], and the standardized delayed-mode quality control
91 procedures [Maurer et al., 2021]. Together, these developments have reduced uncertainty and
92 improved the consistency of optode-based [O₂] measurements from Argo floats.

93

94 To date, oxygen observations from Argo floats have been used primarily in regional process studies,
95 including air-sea oxygen exchange [Wolf et al., 2018], upper-ocean primary production [Alkire et al.,
96 2012; Estapa et al., 2019], biological pump efficiency [Johnson and Bif, 2021], and the dynamics of
97 the oxygen minimum zone [Udaya Bhaskar et al., 2021]. Recently, Sharp et al. [2023] produced a

98 four-dimensional gridded [O₂] product, GOBAI-O₂ (Gridded Ocean Biogeochemistry from Artificial
99 Intelligence (AI) – Oxygen). GOBAI-O₂ is constructed using machine-learning methods trained on
100 oxygen observations and designed to reconstruct spatial patterns, seasonal cycles, and decadal
101 variability, particularly in regions where observational data gaps coincide with high background O₂
102 variability.

103

104 In the North Pacific, several studies have documented heterogeneous oxygen trends. Using an
105 objectively mapped monthly climatology of O₂ based on the World Ocean Database 2013 (WOD13)
106 [Boyer et al. 2013], Ito et al. [2017] reported multidecadal variability and trends in dissolved O₂ in
107 the surface-layer oxygen from 1958 to 2013. Sasano et al. [2015], using the high-frequency shipboard
108 sections along the 137°E and 165°E lines from 1987 to 2011, reported oxygen declines in the northern
109 subtropical to subtropical-subarctic transition zones of $-0.45 \pm 0.16 \mu\text{mol/kg/yr}$ at 25.3 σ_{θ} and $-0.45 \pm$
110 $0.14 \mu\text{mol/kg/yr}$ at 26.8 σ_{θ} , respectively. They also identified a significant oxygen increase in the
111 tropical Oxygen Minimum Layer (OML) of $+0.36 \pm 0.004 \mu\text{mol/kg/yr}$, highlighting pronounced spatial
112 heterogeneity in oxygen trends. At broader scales, Stramma et al. [2020] analyzed historical bottle
113 data and reported links between oxygen variability and climate modes such as the Pacific Decadal
114 Oscillation (PDO) and the North Pacific Gyre Oscillation (NPGO), although sparse sampling makes
115 it difficult to robustly connect regional trends to physical mechanisms. Collectively, previous studies
116 indicate that oxygen changes in the North Pacific can be strong, spatially non-uniform, and potentially
117 driven by both circulation/ventilation changes and biologically mediated oxygen consumption
118 [Sasano et al. 2015; 2018; Ito et al. 2017; 2024; Stramma et al., 2020; Kolodziejczyk et al. 2024].

119

120

121 Because observational opportunities to quantify trends in dissolved oxygen—together with concomitant
122 changes in temperature and salinity—remain limited, gridded products such as GOBAI-O₂ are

123 becoming increasingly valuable for basin-scale analyses. In this study, we use GOBAI-O₂ to quantify
124 linear trends in potential temperature, salinity, and dissolved oxygen in the North Pacific over 2004–
125 2023 and examine how their trends are connected in both depth and density space. We further discuss
126 the extent to which the diagnosed oxygen trends can be interpreted in terms of physical drivers,
127 including surface warming, stratification changes, and circulation variability in the North Pacific.

128

129 **2. Data and Methods**

130 **2.1 GOBAI-O₂ dataset**

131 We use GOBAI-O₂ (Version 4.4), a four-dimensional, monthly gridded product of dissolved oxygen
132 (O₂) in the ocean interior, generated using machine learning (ML) algorithms trained on both Argo
133 float oxygen measurements and ship-based discrete observations [Sharp et al., 2023]. GOBAI-O₂ is
134 mapped onto the temperature-salinity fields provided by the global Argo array [Roemmich and Gilson,
135 2009]. The underlying oxygen training database combines ship-based measurements from
136 GLODAPv2.2022 and Argo float data distributed through the Argo Global Data Assembly Centers,
137 after quality control [Sharp et al., 2023] (<https://doi.org/10.25921/z72m-yz67>).

138

139 According to Sharp et al. [2023], the float data used in GOBAI-O₂ were filtered to retain only delayed-
140 mode adjusted profiles with quality flags of 1 (good), 2 (probably good), or 8
141 (interpolated/extrapolated) for pressure, temperature, salinity, and dissolved oxygen. Among all
142 available float profiles, 51.4% underwent quality control through comparison with climatological
143 fields from the World Ocean Atlas (WOA) or the Commonwealth Scientific and Industrial Research
144 Organisation Regional Sea Atlas (CARS). An additional 30.3% were evaluated using atmospheric
145 oxygen concentration measurements, and 7.0% were quality controlled through comparison with in-
146 water measurements (WOD, OMS assuming an oxygen zero, or deployment-time CTD profiles). A

147 further 5.3% were adjusted using in-situ optode calibration based on the method of Drucker and Riser
148 [2016], 3.3% were adjusted by other methods, 1.9% were unclassified, and the remaining 0.9% were
149 not adjusted.

150

151 The ML models predict O₂ using predictors that include absolute salinity, conservative temperature,
152 potential density anomaly, hydrostatic pressure, bottom depth, and additional spatiotemporal
153 covariates representing geographic, seasonal, and interannual variability. Biological processes are not
154 explicitly parameterized in the ML framework; however spatiotemporal covariates can implicitly
155 capture biological influences to some extent [Giglio et al., 2018].

156

157 GOBAI-O₂ is produced using two ML approaches: feed-forward networks (FNNs) and random forest
158 regression (RFRs, [Breiman, 2001]). The final O₂ estimate at each grid point is taken as the mean
159 of the FNN and RFR predictions. The dataset spans 2004–2023 at monthly resolution on a 1° × 1°
160 latitude –longitude grid, covering 86% of the global ocean area. The product is provided on 58 vertical
161 levels from the surface to ~2,000 m. Sharp et al. [2023] reported 0.79 ± 0.04% per decade decrease
162 in the oxygen inventory of the upper 2000 m over 2004–2022. Full details of their data sources,
163 processing, algorithm training, evaluation, and uncertainty estimation are given in Sharp et al. [2023].

164

165 **2.2 Uncertainty estimates**

166 GOBAI-O₂ provides an uncertainty estimate for each gridded O₂ value, constructed by combining
167 independent uncertainty components in quadrature [Sharp et al., 2023]:

$$168 \quad u([O_2])_{tot.} = \sqrt{u([O_2])_{meas.}^2 + u([O_2])_{grid.}^2 + u([O_2])_{alg.}^2} \quad (1),$$

169 where $u([O_2])_{meas.}^2$ represents measurement uncertainty of the underlying observations,

170 $u([O_2])_{grid}^2$) is the gridding uncertainty associated with representing a four-dimensional
171 spatiotemporal volume by a single value, and $u([O_2])_{alg}^2$ is the algorithmic uncertainty arising from
172 the ML estimation. We use $u([O_2])_{tot}$ to characterize uncertainty in O_2 and to propagate uncertainty
173 into our oxygen trend estimates (Figs. 1–4). In most figures, we incorporate the mean uncertainty when
174 estimating linear O_2 trends.

175

176 **2.3 Vertical grid and interpolation for isopycnal analysis**

177 GOBAI- O_2 is provided on a $1^\circ \times 1^\circ$ horizontal grid with 58 depth levels: 2.5, 10, 30, 40, 50, 60, 70,
178 80, 90, 100, 110, 120, 130, 140, 150, 160, 170, 182.5, 200, 220, 240, 260, 280, 300, 320, 340, 360,
179 380, 400, 420, 440, 462.5, 500, 550, 600, 650, 700, 750, 800, 850, 900, 950, 1000, 1050, 1100, 1150,
180 1200, 1250, 1300, 1350, 1412.5, 1500, 1600, 1700, 1800, 1900 and 1975 m. The enhanced near-surface
181 vertical resolution is important for resolving strong gradients in temperature, salinity, density, and
182 oxygen within the mixed layer [Kara et al., 2000].

183

184 For analysis performed in density space, we interpolate the original depth-level data to 1-m vertical
185 grid using cubic spline interpolation and then evaluate linear trends on a $1^\circ \times 1^\circ \times 1$ m grid. This
186 approach enables computation of trends as a function of latitude (1° bins) and potential density
187 anomaly ($0.1\sigma_\theta$ bins) (Figs. 4–7). To evaluate sensitivity to interpolation choices, we repeated the
188 analysis using linear, shape-preserving cubic (PCHIP) interpolation and using coarser vertical grids
189 (2 m and 5 m). The resulting trend patterns show no material differences among interpolation methods
190 (Figs. S1 (a, b) and S2 (a, b)). The 5-m grid cannot resolve densities lighter than $24.0\sigma_\theta$ at some
191 latitudes; however, the main features are preserved across all tested resolutions.

192

193 **2.4 OFES model output**

194 In Section 3.3.2, we additionally use output from the eddy-resolving OGCM for the Earth Simulator
195 (OFES) [Masumoto et al., 2004; 2010; Sasaki et al., 2008] to examine the physical context of the
196 diagnosed variability. OFES is based on the MOM3 [Pacanowski and Griffies, 2000] and uses a quasi-
197 global domain spanning 75° S– 75°N with 0.1° x 0.1° horizontal resolution and 54 vertical levels. The
198 model was initialized from rest using the World Ocean Atlas 1998 (WOA98) [Boyer and Levitus,
199 1997], and spun up for 50 years using climatological forcing derived from NCEP-NCAR reanalysis
200 [Kalnay et al., 1996]. After spin-up, a hindcast experiment was conducted from 1950 to 2024 using
201 daily NCEP-NCAR forcing. Here we analyze OFES output over 1950–2023.

202

203 **2.5 GODAS model output**

204 In Section 3.3.2, we also use temperature and salinity fields from the NCEP Global Ocean Data
205 Assimilation System (GODAS) to complement our analysis. GODAS is a global ocean reanalysis
206 system developed at the National Centers for Environmental Prediction (NCEP) and is based on the
207 Modular Ocean Model version 3 [Pacanowski and Griffes, 2000]. The system assimilates surface
208 temperature profiles, XBT data, moored buoy observations, and other in situ measurements using a
209 three-dimensional variational (3DVAR) assimilation scheme [Behringer and Xue, 2004; Behringer,
210 2007]. The GODAS reanalysis is provided on a 1° x 1° horizontal grid with enhanced meridional
211 resolution (1/3°) near the equator and includes 40 vertical levels. The reanalysis spans from 1980 to
212 the present and is widely used for climate diagnostics and ocean variability studies. In this study, we
213 analyze GODAS density fields over the period 2003-2024 by using temperature and salinity.

214

215 **3. Results**

216 **3.1 Horizontal distributions of linear trends**

217 Figure 1 illustrates the horizontal and vertical distributions of linear trends in potential temperature,

218 salinity, and dissolved oxygen (O_2), over 2004–2023. Positive trends in potential temperature are
219 primarily confined to the surface layer above 200 m depth (Fig. 1a–c), with larger magnitudes at
220 higher latitudes. In contrast, negative trends emerge below the surface in the eastern tropical area
221 (180° – 120° W, 5° – 15° N) (Fig. 1b), extending westward and deepening with increasing depth (Fig.
222 1d–f). Below \sim 400 m, the spatial distributions of positive and negative temperature trends differ
223 between the subarctic and subtropical gyres.

224

225 Salinity trends exhibit generally negative values throughout the surface layer (Fig. 1h–i), consistent
226 with freshening. Localized positive salinity trends are detected in the Kuroshio–Oyashio transition
227 area and the northwest Pacific (140° – 180° E, 20° – 50° N), as well as in the tropical region (120° –
228 170° E, 0° – 10° N). Additional positive trends are observed along the eastern boundary off California
229 (130° – 199° W, 20° – 40° N). Below 200 m depth, salinity trends are weaker and broadly mirror the
230 temperature (Fig. 1j–k). Notably, negative salinity trends are evident around the Alaska gyre (170° –
231 130° W, 40° – 55° N) (Fig. 1j–l), a pattern that differs from the corresponding temperature trends.

232

233 Negative trends in dissolved O_2 are widespread across the North Pacific and extend throughout much
234 of the water column (Fig. 1o–u). Large negative trends are concentrated at higher latitudes near the
235 surface, with their locations shifting systematically with depth. Particularly strong O_2 declines are
236 observed along the northeastern boundary (140° – 130° W, 40° – 50° N) and within the southern
237 subtropical region (10° – 25° N) on density surfaces between 25.2 and $26.8\sigma_\theta$, corresponding to depths
238 of approximately 200–600 m (Fig. 1q–s). In contrast, weak positive O_2 trends are detected below 200
239 m depth in the Kuroshio–Oyashio transition zone (130° – 150° E, 30° – 40° N), extending into deeper
240 layers and spreading northeastward across the basin (Fig. 1r–u).

241

242 Positive O_2 trends are restricted to specific regions and depths: the tropical region at ~ 100 m depth
243 (Fig. 1p); the Alaska Gyre at 200–400 m depth (Fig. 1q–r); the western tropical region at 400–600
244 m depth (Fig. 1r–s); and the Kuroshio–Oyashio transition region at similar depths (Fig. 1r–s). When
245 examined as a function of latitude, the magnitudes of negative O_2 trends do not depend monotonically
246 on latitude alone. While surface-layer declines are strongest at high latitudes, the largest negative
247 trends at intermediate depths (400–600 m) occur in the mid-latitude band (30° – 40° N). This depth-
248 dependent latitudinal structure implies the importance of remote transports and the circulation-driven
249 redistribution of oxygen, rather than purely local surface forcing. The underlying mechanisms are
250 discussed further in Section 3.3.

251

252 The total uncertainty in dissolved O_2 , $u([O_2])_{tot.}$, exhibits pronounced regional structure (Fig. 2a–
253 g). Uncertainty is largest in the North Pacific north of 50° N and decreases toward lower latitudes.
254 Relatively high uncertainty values are also evident in the surface layer, and within regions of strong
255 density gradients in the eastern tropical Pacific [150° – 120° W, 10° – 30° N] at depths of 100–200 m (Fig.
256 2b–c). In general, uncertainty peaks near 100 m depth and decreases with increasing depth (Fig. 2
257 and Figure A14 in Sharp et al. [2023]). As shown by Sharp et al. [2023], regional variations in
258 uncertainty are dominated by algorithmic uncertainty rather than measurement or gridding components
259 (Eq. 1). Elevated algorithmic uncertainty in the northern Pacific above 50° N and along the western
260 and eastern tropical margins below 20° N reflects sparse observational coverage in these regions
261 (Figure 1 in Sharp et al. 2023).

262

263 To assess whether regional trends exceed the dataset uncertainty, we computed the spatial distribution
264 of Robustness (R), defined as $R = |\text{trend over two decades}| / \text{uncertainty}$ (Fig. 1v–bb). (Note: This
265 diagnostic provides a heuristic measure of the relative strength of the trend compared to the local

266 uncertainty, rather than a formal quantification of uncertainty propagation.) The results indicate that R
267 exceeds or approaches high values in the eastern and western tropical zones, the Kuroshio Extension
268 region, portions of the subpolar North Pacific, and along the 27.2–27.4 σ_θ density surfaces at 800–
269 1000 m depth. Based on this metric, larger oxygen trend magnitudes correspond to higher R values,
270 more clearly distinguishable from the background uncertainty. Thus, in the upper ocean (2.5–100 m),
271 trends are relatively robust in terms of the R metric, mainly in the northern North Pacific. At 200–400
272 m, robust signals appear both in the northern North Pacific and along the 25.2–26.0 σ_θ surfaces in the
273 southern subtropical region, as well as in the eastern and western tropics. At 600–1000 m, the trends
274 are robust within the subtropical gyre bounded by the 27.0 σ_θ surface.

275

276 Compared with the previously reported historical horizontal distributions of dissolved O₂ reported by
277 Ito et al. [2017] (Figure 3 in Ito et al. 2017), our analysis shows a broader spatial extent of negative
278 trends across the North Pacific. Whereas data gaps increase with depth in Ito et al. [2017], the GOBAI-
279 O₂ product provides more spatially continuous coverage, yielding distributions that are consistent with
280 surrounding regions. In addition, positive O₂ trends detected here in the Kuroshio–Oyashio transition
281 zone and the northeastern North Pacific on density surfaces of 26.8–27.0 σ_θ (Fig. 1r) were not clearly
282 evident in the earlier O₂ anomaly analysis. Similarly, the positive trends identified in the western
283 tropical Pacific below 400 m depth (Fig. 1r–t) are stronger and more spatially coherent than those
284 reported previously.

285

286 The positive O₂ trends coincide with regions of relatively low uncertainty values (Fig. 1p–s and 1w–
287 z), suggesting that they represent relatively robust features that are better constrained by the high
288 observation density of Argo profiling floats. Other regions exhibiting positive signals—the

289 northeastern North Pacific with a density range of $26.8\text{--}27.0\sigma_\theta$ ($170^\circ\text{E}\text{--}150^\circ\text{W}$, $45\text{--}55^\circ\text{N}$, Fig. 1r)
290 and the tropical western Pacific ($130^\circ\text{--}170^\circ\text{E}$, $0^\circ\text{--}10^\circ\text{N}$, Fig. 1r-t)—also correspond to areas of low
291 uncertainty (Fig. 1y-aa). Consequently, these signals may reflect possible regional reoxygenation
292 superimposed on the basin-scale deoxygenation trend.

293

294 Some localized expansions of the trend patterns, particularly in the tropical eastern Pacific (e.g. 170°--
295 130°W , $0^\circ\text{--}20^\circ\text{N}$) may partly reflect regions of elevated uncertainty, occasionally exceeding 15
296 $\mu\text{mol/kg}$ (Fig. 1q-s; Fig. 4i). Such large uncertainties would likely arise from sparse observations and
297 high background variability [Sharp et al. 2023]. Additional bias may stem from sensor calibration
298 limitations in Argo oxygen measurements, especially in oxycline regions where finite optode response
299 times can introduce systematic errors [Bittig et al., 2014; 2018a,b]. Despite these caveats, the spatial
300 patterns of the diagnosed O_2 trends are generally smooth and coherent across the basin. Based on
301 statistical significance testing, most trends are significant throughout the water column (Fig. 1o-u).
302 Overall, despite the uncertainties associated with the various factors discussed above, the GOBAI- O_2
303 dataset provides an improved framework for diagnosing basin-scale oxygen variability and its physical
304 drivers.

305

306 **3.2 Vertical sections and isopycnal density analysis of linear trends in 137°E and 165°E lines**

307 To facilitate direct comparison with historical ship-based observations, we examine vertical sections
308 and isopycnal distributions of linear trends in potential temperature, salinity, and dissolved O_2 along
309 the 137°E and 165°E meridional sections (Fig. 3). Ogata and Nonaka [2020] analyzed salinity data
310 from 20 years of shipboard observations along the 137°E line between 1997 and 2016, while Sasano
311 et al. [2015] analyzed temperature, salinity, and dissolved O_2 data from 25 years of cruises along the

312 165°E line between 1987 and 2011.

313

314 Along both sections, large negative trends in potential temperature and salinity are concentrated along
315 the 25.0–26.0 σ_θ isopycnal surfaces, corresponding to potential temperatures of approximately 10–
316 12°C and salinities of 34.4–34.5 (Fig. 3a, b, e, f). In contrast, the strongest negative trends in dissolved
317 O₂ occur primarily along denser isopycnals between 26.0 and 27.0 σ_θ (Fig. 3c, g). This vertical
318 separation indicates that the regions of pronounced oxygen decline are not co-located with those of
319 temperature and salinity trends, implying distinct controlling mechanisms.

320

321 In addition to widespread oxygen declines, pronounced positive O₂ trends are detected south of ~15°N
322 below 200 m depth along the 137°E line (Fig. 3c). These positive trends are located near the upper
323 boundary of the oxygen minimum layer (OML). Comparison with the corresponding uncertainty
324 distributions (Fig. 3d, h) shows that regions exhibiting positive or negative oxygen trends generally
325 do not coincide with areas of elevated uncertainty, indicating that these signals are robust within the
326 GOBAI-O₂ framework.

327

328 The distributions of linear trends on isopycnal surfaces further highlight differences among
329 temperatures, salinity, and dissolved O₂ (Fig. 4). Trends in temperature and salinity are closely aligned,
330 with warming accompanied by salinification and cooling accompanied by freshening (Fig. 4a–b, d–
331 e). In the tropical region (5°S–5°N), distinct positive trends in both variables are evident over the
332 density range of 22.0–26.0 σ_θ . In contrast, little systematic trend is detected in the salinity minimum
333 region (S = 34–34.1) within the density range of 26.5–27.0 σ_θ . At higher latitudes (40°–50°N), strong
334 positive trends in both temperature and salinity are observed along the 26.0–27.0 σ_θ surfaces (Fig. 4e).

335

336 Dissolved oxygen trends exhibit a markedly different structure. Although negative O_2 trends dominate
337 overall, weak but coherent positive trends appear across the density range $23.0\text{--}26.0\sigma_\theta$ in low-latitude
338 regions ($5^\circ\text{S}\text{--}5^\circ\text{N}$). More pronounced positive O_2 trends are detected in the deeper density range of
339 $26.0\text{--}27.0\sigma_\theta$ between 5° and 10°N . Additional weak positive trends are observed between 10° and
340 20°N within the density range of $23.0\text{--}25.0\sigma_\theta$ along both the 137°E and 165°E sections.

341

342 Compared with previous studies, the GOBAI- O_2 -based trends reveal both similarities and notable
343 differences. The general characteristics of temperature and salinity trends are broadly consistent with
344 those reported by Sasano et al. [2015], although the present results are spatially smoother, particularly
345 for dissolved oxygen. This smoothness likely reflects the gridded nature of the dataset and the spatial
346 regularization inherent in the machine-learning reconstruction. Along the 137°E section, the GOBAI-
347 O_2 temperature and salinity fields exhibit a wider area of negative salinity trends within the density
348 range $22.0\text{--}24.0\sigma_\theta$ than those reported by Ogata and Nonaka [2020] using OFES output.

349

350 Ship-based observations by Sasano et al. [2015] identified patchy positive trends in oxygen within
351 the density range $24.5\text{--}27.5\sigma_\theta$ in the regions ($5^\circ\text{--}15^\circ\text{N}$ and $6^\circ\text{S}\text{--}1^\circ\text{N}$), as well as localized positive
352 trends at greater depths. In contrast, the GOBAI- O_2 data reveal a broader, smoother, and more spatially
353 coherent pattern of positive O_2 trend spanning 6°S to 5°N . At the same time, the present analysis more
354 clearly delineates the core regions of negative oxygen trends between 5° and 15°N along the lower
355 isopycnals (Fig. 3c and f), which are characteristic of the subtropical gyre. These differences
356 underscore the complementary nature of ship-based observations and gridded reconstructions and
357 highlight the advantage of GOBAI- O_2 for resolving basin-scale and isopycnal-scale oxygen variability.

358

359 **3.3 Horizontal distribution of linear trends along isopycnal surfaces**

360 3.3.1 Potential temperature and salinity

361 The horizontal distributions of linear trends in potential temperature, salinity, and dissolved oxygen on
362 specific isopycnal surfaces at 25.0, 26.0, and 26.8 σ_θ (Fig. 5) are illustrated to examine how these
363 trends occur and how they are connected. These density surfaces correspond to the shallower density
364 range of Subtropical Mode Water (STMW), the shallower densities of Central Mode Water (CMW)
365 [Suga et al., 1997; 2004], and the representative density of North Pacific Intermediate Water (NPIW)
366 [Nakamura et al., 2000a, b; Nakamura and Awaji, 2003; Yasuda, 2004], respectively. STMW is
367 formed south of the Kuroshio Extension between 30–35°N and 130–170°E, and reaches depths of
368 approximately 400 m in late winter. It then spreads toward the subtropical front through advection
369 across the Kuroshio recirculation area. CMW is formed in the transition area of the central North
370 Pacific and spreads eastward along the North Pacific Current before turning southward and westward
371 in the subtropical gyre [Suga et al., 1997; 2004]. In contrast, NPIW does not outcrop during its
372 formation process. Its origin lies in Okhotsk Sea Mode Water, which forms through overturning driven
373 by diapycnal upwelling and tidal mixing around the Kuril Islands [Nakamura et al., 2000a, b;
374 Nakamura and Awaji, 2003; You, 2003; Yasuda, 2004] as well as double diffusions in the North Pacific
375 [You, 2003].

376

377 The linear trends on the 25.0, 26.0, and 26.8 σ_θ surfaces show that positive and negative tendencies
378 appear in characteristic locations and are generally aligned with the geostrophic streamlines (Fig. 5a–
379 b, d–e, g–h). Although exceptions exist, such as weak positive trends (150–175°E, 20–30°N) (Fig.
380 5a–b), negative trends in potential temperature and salinity dominate in the western and central North
381 Pacific on the 25.0 and 26.0 σ_θ surfaces (Fig. 5a–b, d–e). Conversely, positive trends in temperature
382 and salinity are most prevalent in the northeastern and/or eastern regions of the basin along the
383 geostrophic streamlines (Fig. 5a–b, d–e). These patterns suggest that waters subducted in the frontal
384 region with reduced temperature and salinity originate mainly from the northeastern North Pacific and

385 are advected southward along the subtropical circulation (Fig. 5a–b, d–e). Exceptions occur in parts
386 of the northeastern basin (170–130°W, 40–60°N), where warmer and more saline waters influence
387 the water masses sinking near the Alaska gyre and subsequently transported outside the subtropical
388 gyre and along the California coast.

389

390 At $26.8\sigma_\theta$ (Fig. 5g–h), large positive trends in temperature and salinity are found along the Kuril
391 Islands, with moderate positive trends appearing on the eastern side of the basin, respectively. Waters
392 at this density range ($26.8\sigma_\theta$) are not directly ventilated but are formed through diapycnal mixing
393 processes [Nakamura et al., 2000a, b; Nakamura and Awaji, 2003; You, 2003; Yasuda, 2004] and
394 through double diffusion such as salt fingering [You, 2003]. Thus, the observed positive temperature
395 and salinity trends at $26.8\sigma_\theta$ likely reflect influences from changes occurring in the overlying layers
396 (Fig. 5d–e and g–h).

397

398 A meridional northward shift of the outcrop line in the North Pacific associated with recent climate
399 change has been documented in OFES analyses [Ogata and Nonaka, 2020] and in other observational,
400 reanalysis, and eddy-resolving ocean hindcasts [Xu et al., 2022]. Consistent with these studies, the
401 present dataset exhibits clear northward migration of the $25.0\sigma_\theta$ and $26.0\sigma_\theta$ outcrop lines (Fig. 6a),
402 with the strong shifts occurring in the eastern basin between 150°E and 180°W (Fig. 6 and Table 1).
403 The estimated northward shift rate at $0.004\text{--}0.09\text{ }^\circ\text{yr}^{-1}$ from 2004 to 2023 is comparable to the value of
404 $0.04\text{ }^\circ\text{yr}^{-1}$ reported by Xu et al. [2022] for 1980 to 2018. Xu et al. [2022] further demonstrated that
405 changes in the mixed layer and outcrop lines are tightly coupled with the northward migration of the
406 North Pacific subtropical gyre and KE/OE fronts due to the poleward expansion of the Hadley cell,
407 including the fact that the Kuroshio Extension and Oyashio Extension fronts, mode waters, and
408 subtropical fronts evolve as a coherent system. These changes may also reflect the influence of

409 anthropogenic warming, which has been linked to the poleward expansion of the Hadley circulation
410 and the associated meridional shifts of oceanic fronts [Yang et al., 2020].

411

412 Such poleward displacements of frontal structures can help explain the negative temperature and
413 salinity trends in the subtropical gyre, where less saline subarctic-origin waters are subducted and
414 advected southward. The positive temperature and salinity trends occurring in the Alaska region
415 [160°–130°W, 30°–60°N] (Fig. 5a–b and d–e) are likewise consistent with the direct surface
416 warming. In contrast, the 26.0 σ_θ front exhibits primarily longitudinal, rather than meridional, shifts
417 between 2004 and 2023 (Fig. 6), suggesting that the associated temperature and salinity changes arise
418 mainly from direct surface warming and freshening, rather than from density-compensated shifts in
419 water-mass distribution.

420

421 **3.3.2 Dissolved oxygen**

422 The linear trends in dissolved oxygen on the isopycnal surfaces at 25.0, 26.0, and 26.8 σ_θ exhibit
423 predominantly negative values across the North Pacific (Fig. 5c, f, and i), although their spatial
424 distributions are not uniform. Large negative trends are concentrated in the northeastern and eastern
425 regions and gradually decrease toward the west (Fig. 5c, f, and i). Exceptions occur mainly in the
426 tropics, where notable positive trends are found in the western tropical areas on the 26.0 and 26.8 σ_θ
427 surfaces.

428

429 The temporal changes in dissolved oxygen (O₂) were decomposed following the method of Sasano et
430 al. [2015]. The processes underlying the oxygen tendency equations (Eqs. 2 and 3) are summarized
431 below. We evaluated each contributing term and examined its relative importance for the dissolved O₂
432 trends. The total tendency of dissolved oxygen can be expressed as

433
$$\frac{\partial O_2}{\partial t} = \left(\frac{\partial O_2}{\partial z} \frac{\partial z}{\partial t} \right) + \left(\frac{\partial O_2^{sat}}{\partial t} \right)_{net} - \left(\frac{\partial(AOU)}{\partial t} \right)_{net}, \quad (2)$$

434 which can be rearranged as

435
$$\frac{\partial O_2}{\partial t} = \underbrace{\left(\frac{\partial O_2}{\partial z} \frac{\partial z}{\partial t} \right)}_{(i)} + \underbrace{\left(\frac{\partial O_2^{sat}}{\partial t} - \frac{\partial O_2^{sat}}{\partial z} \frac{\partial z}{\partial t} \right)}_{(iii)} + \underbrace{\left(-\frac{\partial(AOU)}{\partial t} + \frac{\partial(AOU)}{\partial z} \frac{\partial z}{\partial t} \right)}_{(v)}. \quad (3)$$

436 (i) (ii) (iii) (iv) (v) (vi)

437 Here, $X = O_2, O_2^{sat}, AOU$ (Apparent Oxygen Utilization). The term $\partial z/\partial t$ denotes the temporal
 438 change in the depth of the isopycnal surface (z), while $\partial X/\partial z$ represents the vertical gradient of the
 439 variable X at that surface, averaged over the past 20 years. The net tendency term $(\partial X/\partial t)_{net}$
 440 represents the net changes associated with a variable X.

441

442 By applying Eq. (3), the rate of O_2 change (term i), which is the rate of reconstructed O_2 data
 443 estimated from the linear regression analysis, on each isopycnal surface can be decomposed into
 444 contributions from:

445 (term ii) vertical heave acting on the vertical O_2 gradient;

446 (term iii) solubility effects due to temperature and salinity changes;

447 (term iv) vertical heave acting on the solubility gradient;

448 (term v) AOU changes related to air-sea disequilibrium, biological activities, and lateral circulation

449 (term vi) vertical heave acting on AOU gradients.

450 The derivation of Eqs. (2) and (3) follows Sasano et al. [2015] and is described in Appendix. A
 451 schematic illustration of this decomposition is provided in Supplementary Figure S5.

452

453 Figure 7 shows the horizontal distributions of the magnitude of each term on 25.0, 26.0, and 26.8 σ_θ
454 surfaces. The results indicate that the prominent O₂ declines (Fig. 5c, f, i) arise from a combination
455 of positive and negative contributions, with the dominant terms varying by latitude. In the high-latitude
456 region around the Alaska Gyre (170°–130°W, 40°–60°N), the largest negative contributions are
457 associated with the deepening of isopycnal surfaces (term ii) and the vertical heave acting on the
458 AOU gradient (term vi) (Fig. 7f, j, k, o). Because the dissolved oxygen generally decreases with
459 depth ($\partial O_2 / \partial z < 0$), deepening of isopycnal surfaces ($\partial z / \partial t > 0$) (Fig. 8 b–c) produces a
460 negative contribution through vertical heave. Similarly, because AOU typically increases with depth,
461 isopycnal deepening leads to an apparent increase in AOU, contributing negatively to dissolved O₂ via
462 term (vi). In contrast, solubility-related changes (term iii) and net AOU tendencies (term v) act in
463 opposite directions during this period (Fig. 7g–h, l–m). Taken together, these results are consistent
464 with the strong negative O₂ trends observed in the Bering Sea on the 26.0 σ_θ and 26.8 σ_θ surfaces
465 (150°E–170°W, 50–60°N; Figs. 5f and i).

466

467 In the subtropical and mid-latitudes (10°–40°N), the O₂ decline is largely associated with AOU
468 changes (term v) (Fig. 7d, i, and n). The relative weakening of the total O₂ decrease in the western
469 North Pacific (Fig. 5c, f, i) coincides with positive contributions from vertical heave of isopycnal
470 surfaces (term ii) (Fig. 7f and k). Additional positive trends arise from solubility-related effects
471 (term iii) (Fig. 7b), and the vertical heave acting on the AOU gradient (term vi) (Fig. 7j and o and
472 Fig. 8b–c).

473

474 In the mid-ocean between 170°E and 160°W, the positive O₂ tendencies transition to weakly negative
475 values. In contrast, a pronounced band of positive trends is found zonally across the North Pacific

476 Ocean between 30°N and 50°N, primarily associated with the combined effects of terms (iii) and (v)
477 (Fig. 7l, h–i, and m–n). This pattern may be related to the northward meridional shift of the subtropical
478 and subarctic frontal zone under recent global warming [Ogata and Nonaka, 2020]. Enhanced winter
479 convection in this region may introduce nutrients into the surface layer, potentially increasing
480 biological activity and AOU. In the NPIW formation region near the Kuril Islands, negative
481 contributions from term (iii) are observed (Fig. 7l), suggesting weaker vertical mixing during the
482 observational period, likely influenced by enhanced surface-layer stratification. This interpretation is
483 supported by the positive trends in temperature and salinity observed in the winter subducted areas
484 [Suga et al., 1997; 2004; Yasuda, 2004] (Fig. 5d–e, g–h).

485

486 In the western tropical Pacific, pronounced increases in dissolved O₂ are observed within the density
487 range of 26.8–27.2 σ_{θ} (Fig. 3c and g; Fig. 4c and g; Fig. 5c, f, and i), overlapping with the OML
488 [Reid, 1997]. Similar features have been reported by Sasano et al. [2015] and Takatani et al. [2012].
489 Variability of the North Equatorial Counter Current (NECC) is likely relevant in this region.
490 According to the study of Chen et al. [2016] based on the OFES outputs including a multidecadal
491 variability (1960–2014), the NECC exhibits two distinct modes of variability: an interannual mode
492 characterized by strengthening accompanied by southward migration, and an interdecadal mode
493 marked by a gradual weakening, poleward migration, and broadening.

494

495 The validity of time-varying signals in the western tropical Pacific in the OFES data has been
496 demonstrated by Chen et al. [2016]. We further examined the longer-term OFES data (1950–2023),
497 as well, for poleward, eastward velocities, as well as potential temperature and salinity here (Fig. 9c,
498 g). Positive temperature anomalies in 0°–5 °N occur above 250 m depth, while negative anomalies

499 appear along the $26.0\sigma_\theta$ surface between 5° – 20° N, a similar pattern that is also evident in the GOBAI-
500 O_2 data (Fig. 3a). A discrepancy is found in salinity trends: GOBAI- O_2 shows negative trends along
501 $26.0\sigma_\theta$ (Fig. 3b), whereas OFES exhibits positive trends (Fig. 9b, f), likely reflecting higher salinity
502 at 200–600 m depth in OFES between 0° and 7° N (Fig. 10b, d).

503

504 Anomalies in poleward and eastward velocities (Fig. 9a–b, e–f and Fig. 11a–b) indicate enhanced
505 poleward flow around 5° N above 200m depth and a poleward shift of the eastward velocity core. These
506 changes are consistent with the interdecadal mode of NECC variability described by Chen et al.
507 [2016]. The broadening of the NECC was less evident here, possibly because the present analysis
508 uses raw velocity fields rather than isolating the second EOF modes. The wind-stress curl over the
509 equatorial Pacific shows a persistent decrease and poleward expansion of negative values along the
510 0° – 10° N from 1950 to 2023 (Fig. 12).

511

512 The westward penetration of the OML is slow and occurs between two eastward-extending tongues of
513 high O_2 water originating near the equator [Reid, 1997] (Fig. S6). The observed O_2 increase on the
514 26.8 – $27.2 \sigma_\theta$ surfaces (Fig. 3c, g and Fig. 4c, g) is consistent with a weakening and northward shift
515 of the interdecadal NECC mode. The subsurface O_2 increase, particularly below 400m depth (Fig. 1r–
516 u), is therefore likely influenced by these circulation changes, potentially allowing higher- O_2 water to
517 extend westward (Fig. S6). In addition, shoaling of isopycnal surfaces near the equator indicates a
518 northward shift of the boundary between the tropical and subtropical gyres along 137° E line during
519 the observational period.

520

521

522 **4. Discussion and Conclusion**

523 The variability of dissolved oxygen in the North Pacific reflects the combined influences of global
524 warming and climate variability. In this study, we used the four-dimensional GOBAI-O₂ dataset,
525 constructed using machine-learning methods applied to historical temperature, salinity, and oxygen
526 observations from BGC-Argo floats and ship-based measurements—to examine linear trends in
527 potential temperature, salinity, and dissolved oxygen over the past two decades (2004–2023). The
528 linear trends are broadly consistent with findings from previous studies [Takatani et al. 2012; Sasano
529 et al. 2015; Ogata and Nonaka, 2020], and we clarified how these trends vary spatially (Figs. 3 and
530 4).

531

532 An important outcome of this study is that GOBAI-O₂, being globally gridded, allows spatially
533 continuous and smooth representations of trends, both horizontally and vertically, across the North
534 Pacific. This provides a more spatially coherent representation than earlier datasets that relied solely
535 on sparse ship-based observations. The horizontal trend patterns mapped on isopycnal surfaces (Fig.
536 5) show that dissolved oxygen exhibits a basin-scale decreasing trend. At the same time, several
537 regions display locally increasing oxygen, including areas influenced by the meridional migration of
538 subtropical and subpolar fronts (Fig. 4). The strong positive oxygen trends in the western equatorial
539 region are consistent with a weakening of the second mode of the NECC variability. The
540 decomposition analysis further illustrates how each physical component contributes to oxygen changes
541 along isopycnal surfaces (Fig. 7).

542

543 Although many of the large-scale features identified here resemble those reported by Ito et al. [2017],
544 our analysis reveals regional and isopycnal-scale structures that were previously unresolved. In

545 particular, the positive oxygen trends in the Kuroshio–Oyashio Transition Zone, the northeastern North
546 Pacific along the 26.8–27.0 σ_θ density surfaces, and the enhanced subsurface O₂ increase in the tropical
547 western Pacific below 400 m were not clearly distinguished in earlier O₂ anomaly studies. These
548 improvements arise because GOBAI-O₂ integrates high-frequency BGC-Argo oxygen observations
549 with a spatially consistent mapping scheme, reducing observational gaps and sampling biases in
550 dynamically active regions. This suggests that regional reoxygenation signals can coexist with large-
551 scale deoxygenation, and highlights the importance of sustained BGC-Argo observations for detecting
552 emerging changes in ocean biogeochemistry.

553

554 Recent work by Bushinsky et al. [2025] has reported the presence of a systematic negative bias
555 (approximately $-2.7 \mu\text{mol kg}^{-1}$) in air-calibrated BGC-Argo oxygen measurements compared with
556 ship-based reference profiles. This bias does not appear to be explicitly corrected in version 4.4 of
557 GOBAI-O₂ and may therefore influence the magnitude of the estimated oxygen trends—potentially
558 enhancing negative trends or suppressing positive ones in regions with dense float sampling. However,
559 as described in Section 2.1, a substantial fraction of these float data is subject to quality control through
560 comparison with climatological fields derived from ship-based discrete observations, and only profiles
561 with appropriate quality flags are retained and incorporated into the dataset development. While this
562 filtering procedure likely mitigates a portion of the air-calibration bias, the extent to which residual
563 bias remains in the reconstructed fields is not well quantified.

564

565 If present, such biases could also affect the apparent vertical structure of the oxycline. In the North
566 Pacific, regions with high float density—such as the Kuroshio–Oyashio transition zone, the North
567 American coastal region, and the vicinity of Hawaii—may be particularly affected (see Fig. 1 of Sharp
568 et al., 2023). While a constant offset would not directly alter linear trend estimates, any time-varying

569 bias associated with sensor behavior or sampling depth could introduce spurious trends. A quantitative
570 evaluation is not feasible at present due to the lack of temporally continuous ship-based reference data
571 at the spatial scales. This limitation should therefore be kept in mind when interpreting the O₂ trends
572 reported here. Accordingly, the interpretation of the diagnosed O₂ trends should be made with caution,
573 particularly in regions where float-based observations dominate.

574

575

576 It is also essential to recognize that GOBAI-O₂ is a machine learning reconstruction derived from
577 available temperature, salinity, and oxygen measurements. While this approach significantly enhances
578 spatial coverage, the results should be interpreted cautiously. In particular, although the large-scale
579 spatial patterns are broadly consistent across datasets, both the magnitude of trends and finer-scale
580 spatial features may still be affected by unresolved observational and reconstruction uncertainties.
581 Nevertheless, future work incorporating improved calibration of Argo oxygen sensors, expanded ship-
582 based reference datasets, independent machine learning reconstructions [e.g., Ito et al., 2024], and
583 comprehensive ocean reanalysis will be necessary to better constrain these uncertainties.

584

585 The monthly mean climatological GOBAI-O₂ dataset should include the Pacific Decadal Oscillation
586 (PDO; Stramma et al., 2020; Pozo Buil and Di Lorenzo, 2017) and the North Pacific Gyre Oscillation
587 (NPGO; Stramma et al., 2020). This dataset, therefore, provides a valuable basis for examining how
588 such climate variability influences dissolved oxygen through physical driving mechanisms.
589 Investigating these relationships more explicitly will be an important direction for future research.

590

591

592 **Data availability:**

593 GOBAI-O₂ data is available at [https://www.ncei.noaa.gov/access/metadata/landing-](https://www.ncei.noaa.gov/access/metadata/landing-page/bin/iso?id=gov.noaa.nodc:0259304)
594 [page/bin/iso?id=gov.noaa.nodc:0259304](https://www.ncei.noaa.gov/access/metadata/landing-page/bin/iso?id=gov.noaa.nodc:0259304). Temperature and salinity are from Roemmich and Gilson
595 [2009] Argo climatology (https://sio-argo.ucsd.edu/RG_Climatology.html). The OFES, NCEP-
596 NCAR, and GODAS data used in our study are obtained from APDRC, University of Hawaii
597 (<http://apdrc.soest.hawaii.edu>).

598

599 **Author contributions:**

600 MI designed the study, performed the analyses, and prepared all figures. MI wrote the initial draft of
601 the manuscript. MI and TO contributed to the interpretation of the results. All authors contributed to
602 improving the manuscript.

603

604 **Acknowledgements:**

605 Jonathan D. Sharp and the reviewers are acknowledged for providing comments that prompted
606 significant improvements to this manuscript.

607

608

609 **Financial support:**

610 This research has been supported by the Institute for Basic Science (grant no. IBS-R028-D1) and the
611 Japan Society for the Promotion of Science (JSPS) through a Grant-in-Aid for Scientific Research
612 JP22H00176.

613

614

615

616

617

618

619

620

621

622

623 **Table captions:**

624 Table 1. Northern shifts of the (outcrop) isopycnal latitudes ($^{\circ} \text{ yr}^{-1}$) for $25.0\sigma_{\theta}$ (a), $26.0\sigma_{\theta}$ (b), and
 625 $26.8\sigma_{\theta}$ (c) in the GOBAI-O₂, OFES, and GODAS datasets. The estimates are based on data from March
 626 of each year. For $26.8 \sigma_{\theta}$, the northern shift is evaluated using the isopycnal depths corresponding to
 627 182, 178m, and 183m in GOBAI-O₂, OFES, and GODAS, respectively.

628 (a) $25.0\sigma_{\theta}$

Longitude	GOBAI-O₂	OFES	GODAS
150 °E	0.0241	0.0157	0.0283
170 °E	0.0444	0.0052	0.0240
170 °W	0.0684	0.0871	0.0481
150 °W	0.0947	0.0353	0.0313
130 °W	0.0420	0.0471	0.0121

629 (b) $26.0\sigma_{\theta}$

Longitude	GOBAI-O₂	OFES	GODAS
150 °E	0.0368	0.0766	0.0358
170 °E	0.0436	-0.0305	0.0508
170 °W	0.0124	0.1997	0.1412

630 (c) $26.8\sigma_{\theta}$

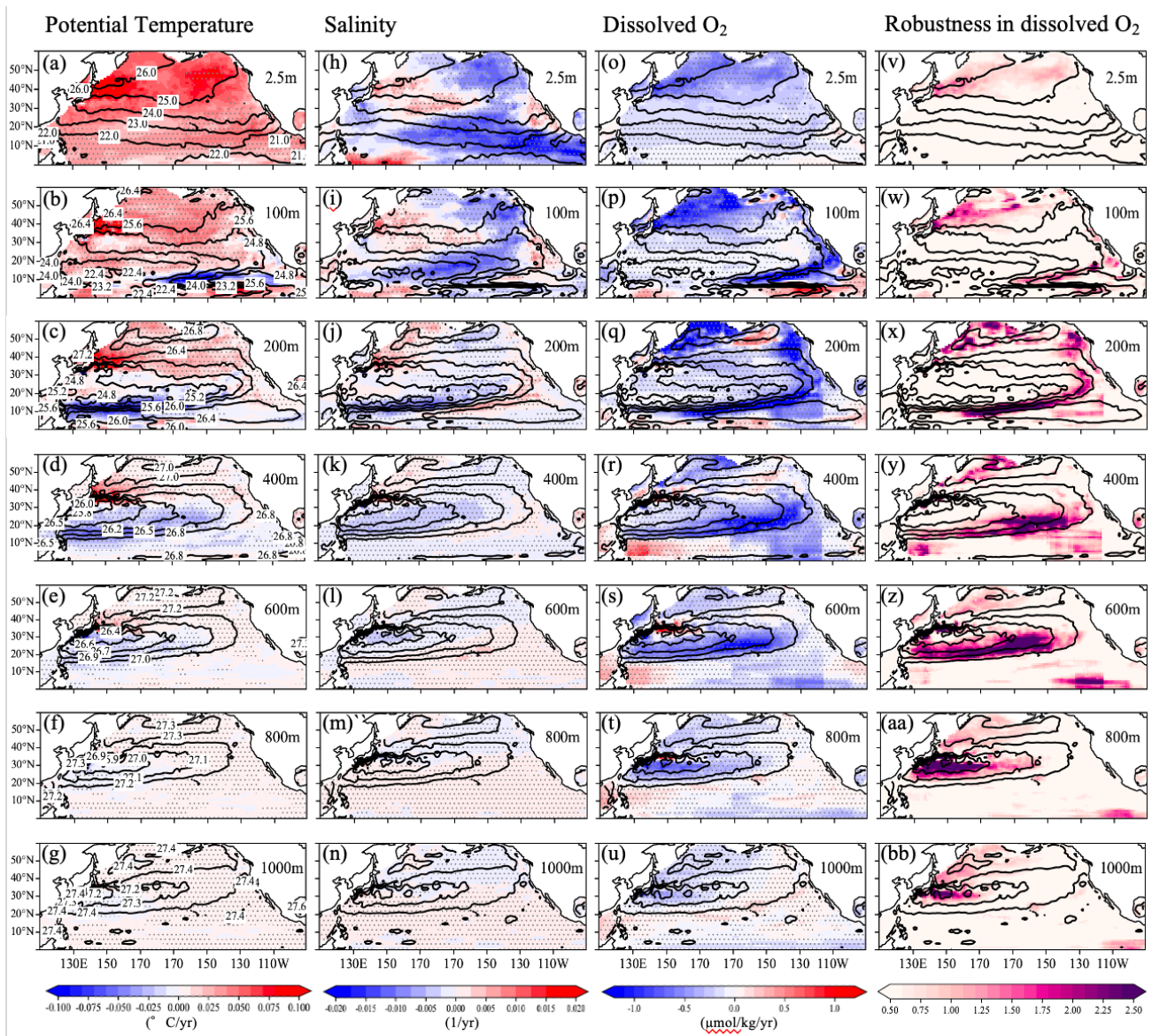
Longitude	GOBAI-O ₂	OFES	GODAS
150 °E	0.0371	0.1980	0.0046
170 °E	0.0338	0.0217	0.1637
170 °W	0.0728	0.0054	0.0261

631

632

633 **Figure captions:**

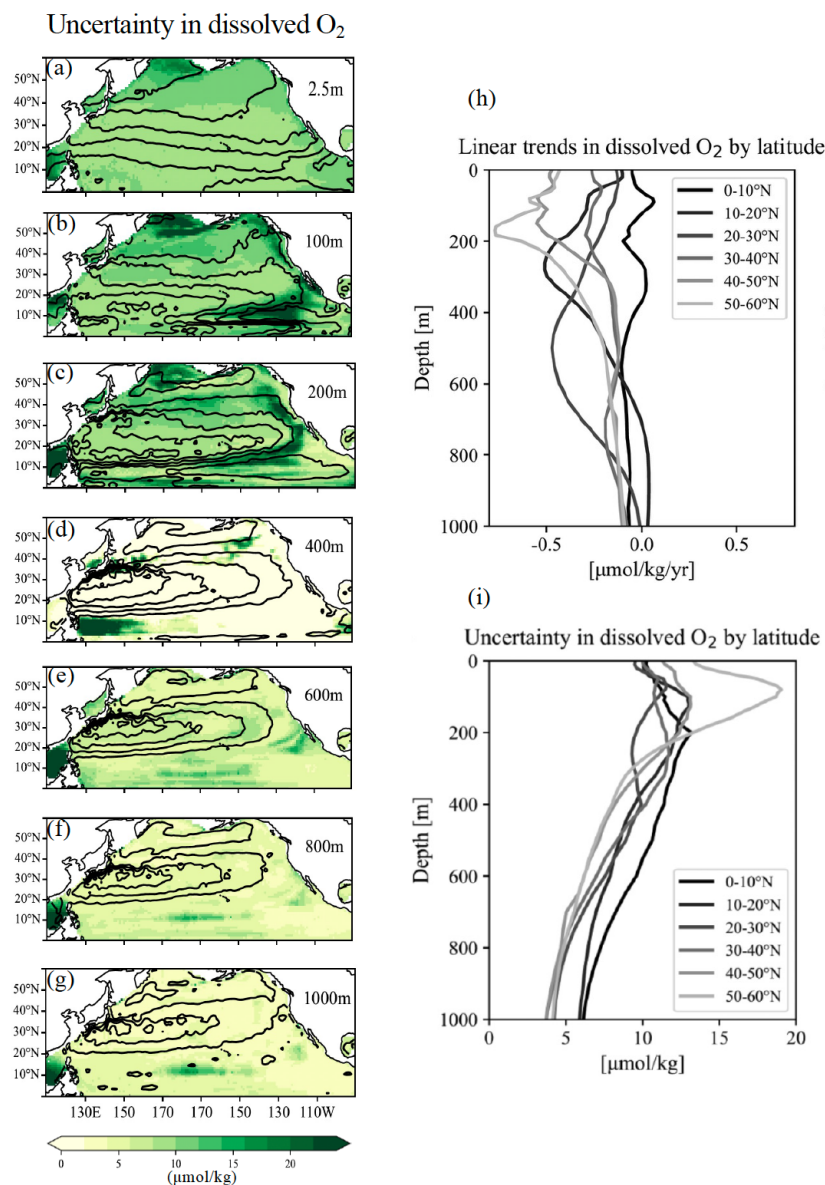
634



635

636 **Figure 1** Horizontal distributions of linear trends in (a–g) potential temperature, (h–n) salinity, and
 637 (o–u) dissolved oxygen (O₂) during the observational period at depths of 0, 100, 200, 400, 600, 800,

638 and 1000 m, respectively. Hatched areas indicate statistically significant trends at the 95% confidence
 639 level based on a Student's t-test with effective degrees of freedom accounting for temporal
 640 autocorrelation. Trend significance was evaluated using a Student's t-test with effective degrees of
 641 freedom accounting for lag-1 autocorrelation. Contours denote potential density at each depth. Labels
 642 for the potential density are shown only in the potential temperature sections. Corresponding
 643 distributions of the Robustness (R), defined as the ratio of the trend magnitude to the dataset
 644 uncertainty in dissolved O_2 are presented in panels (v–bb).
 645

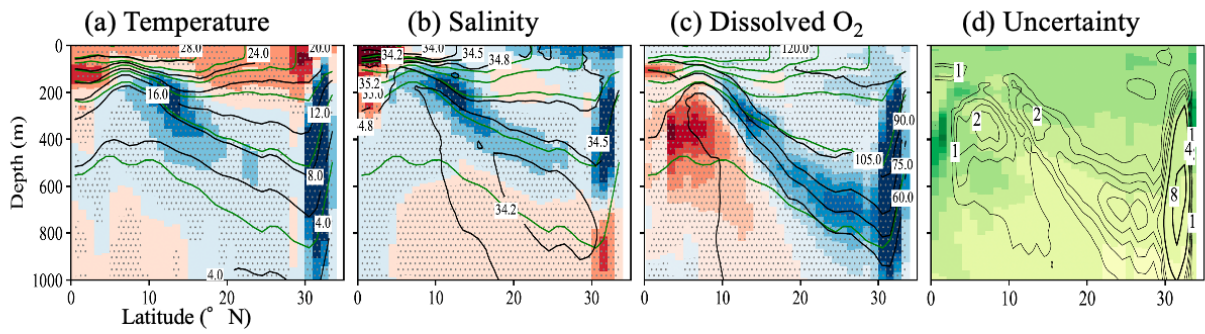


646

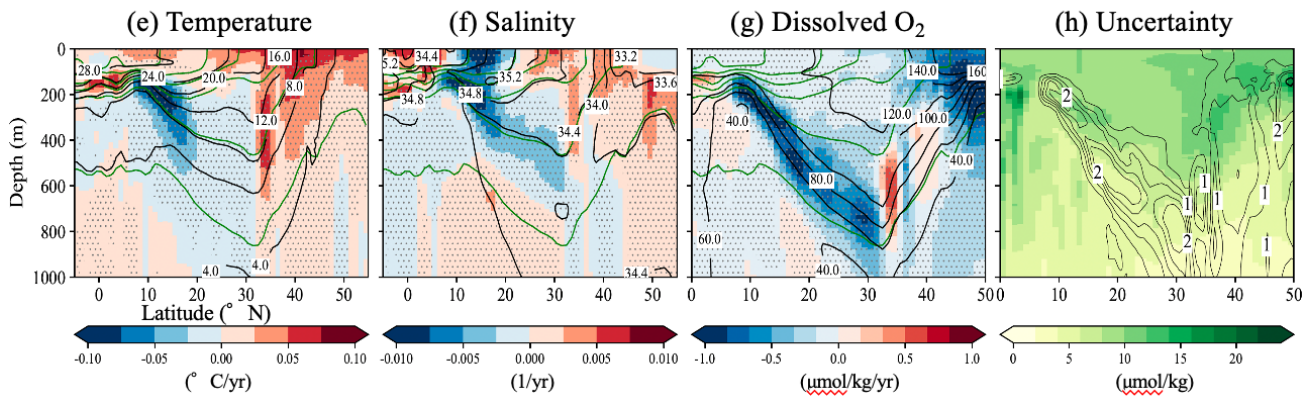
647 **Figure 2** Horizontal distributions of dataset uncertainty in dissolved O_2 (a–g) and vertical profiles of
 648 linear trends and uncertainty in dissolved O_2 by latitude (h–i).

649

137° E line



165° E line

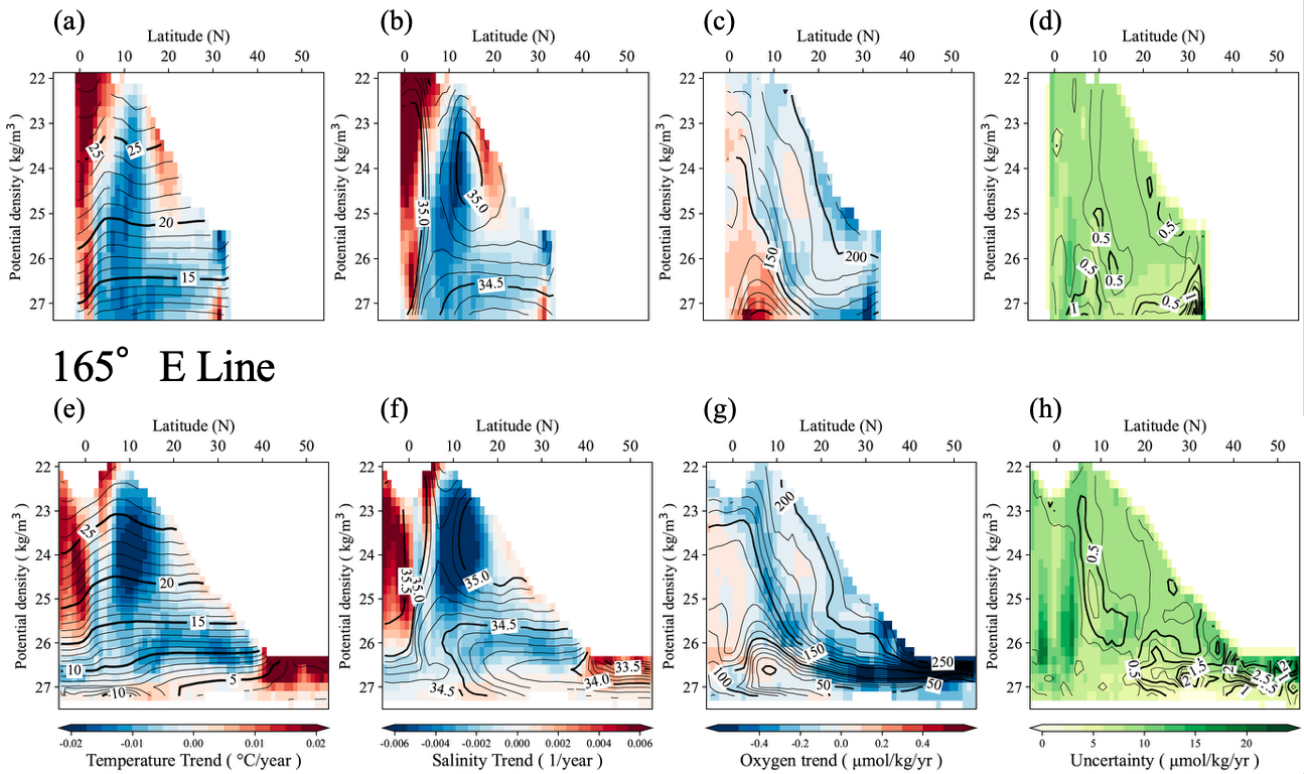


650

651 **Figure 3** Vertical sections showing linear trends in potential temperature (a, e), salinity (b, f), and
 652 dissolved O₂ (c, g) along the 137°E and 165°E meridians, respectively. Black contour lines indicate
 653 the mean potential temperature (a, f), salinity (b, g), and dissolved oxygen (c, h) over the period
 654 2004–2023, while green contour lines represent the mean potential density. Labels for the potential
 655 density are shown only in the robustness sections. Hatched areas indicate statistically significant trends
 656 at the 95% confidence level based on a Student’s t-test with effective degrees of freedom accounting
 657 for temporal autocorrelation. Trend significance was evaluated using a t-test with effective degrees of
 658 freedom accounting for lag-1 autocorrelation. Corresponding vertical sections of the mean uncertainty
 659 with the contours of the Robustness (R) in panels (d, h). The contour intervals for thin and thick
 660 contours in (d, h) are 0.2 and 4.0, respectively.

661

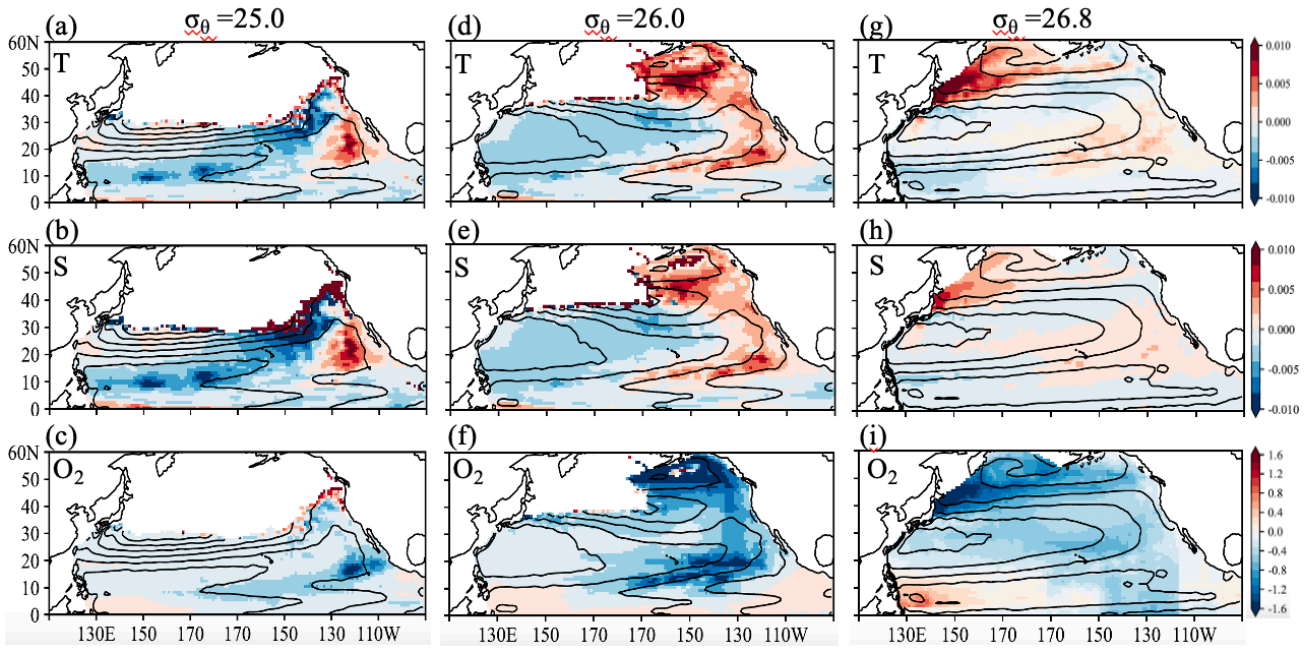
137° E Line



662

663 **Figure 4** Linear trends in (a, e) potential temperature, (b, f) salinity, (c, g), and dissolved O₂ on
 664 each isopycnal surface at intervals of $0.1\sigma_\theta$, calculated at every 1.0 deg of latitude in 137 °E and 165 °E
 665 lines, respectively. Contour lines represent the mean values during the target observation periods,
 666 plotted at intervals of $0.1\sigma_\theta$ for each 1 degree of latitude. Panels (d, h) show the corresponding vertical
 667 sections of mean uncertainty, along with contours of robustness (R). The contour intervals for thin and
 668 thick contours in (d, h) are 0.25 and 0.5, respectively.

669

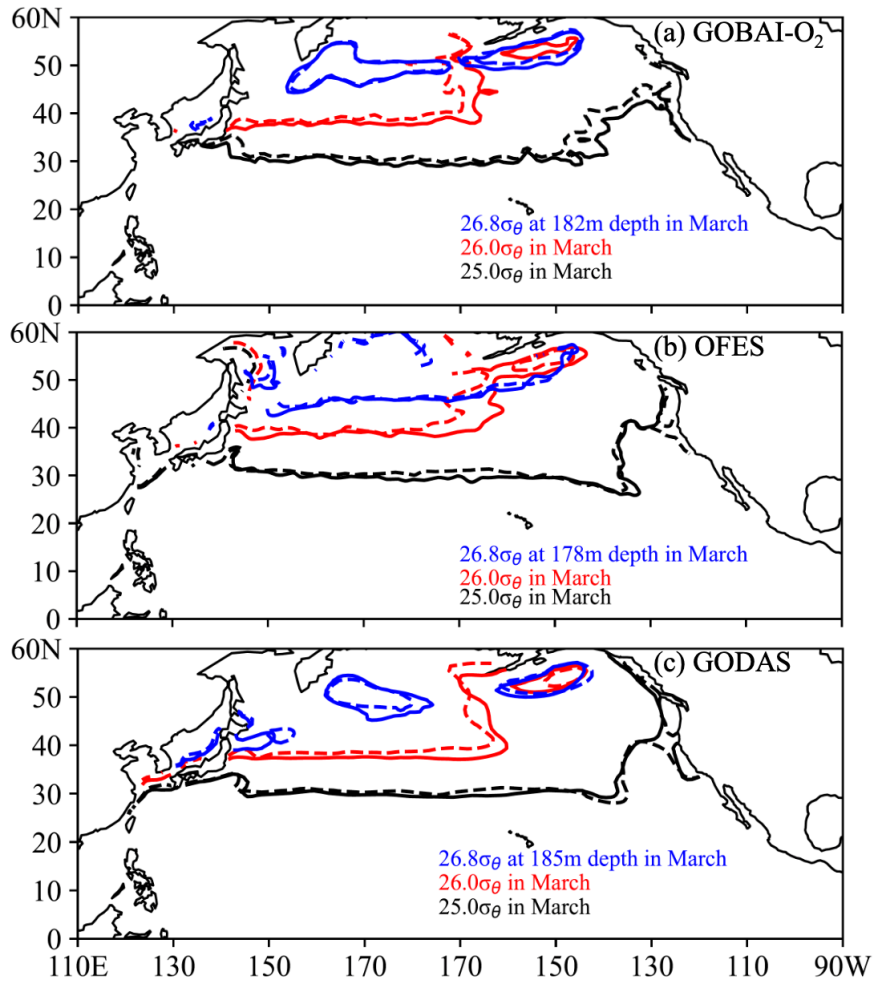


670

671 **Figure 5** Linear trends in (a) potential temperature (°C/yr), (b) salinity (1/yr), and (c) dissolved
 672 O₂ (μmol/kg/yr) on each isopycnal surface at 25.0, 26.0, and 26.8σ_θ. Contour lines represent geostrophic
 673 flow streamlines on 26.0 and 26.8σ_θ surfaces, relative to 2000 m.

674

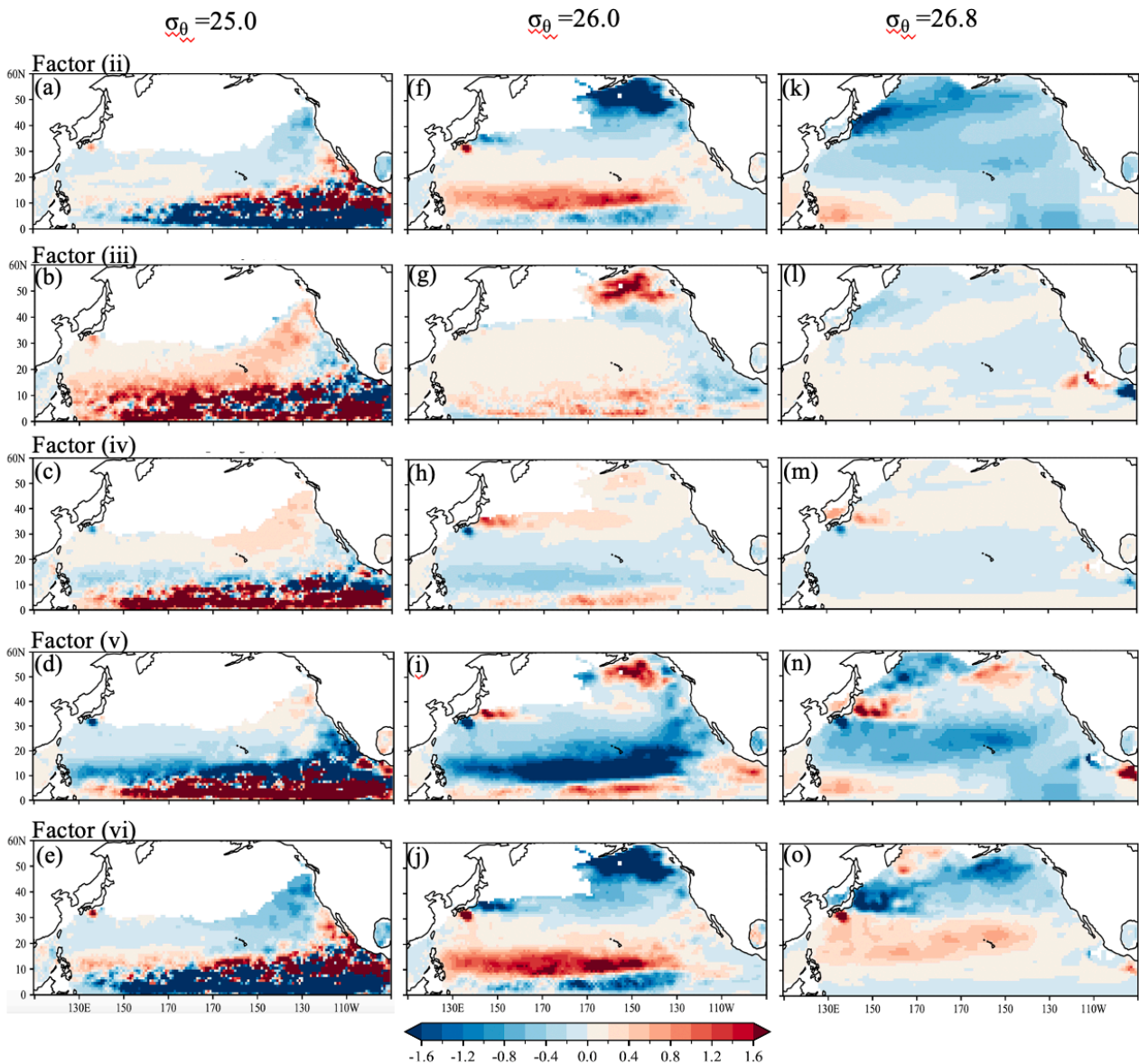
675



676

677 **Figure 6** Density contours of $25.0\sigma_\theta$ (black), $26.0\sigma_\theta$ (red), and $26.8\sigma_\theta$ (blue) in each dataset: (a)
 678 GOBAI-O₂, (b) OFES, and (c) GODAS. Solid lines indicate the mean March density contours for
 679 2004–2009, while dashed lines represent those for 2019–2023.

680

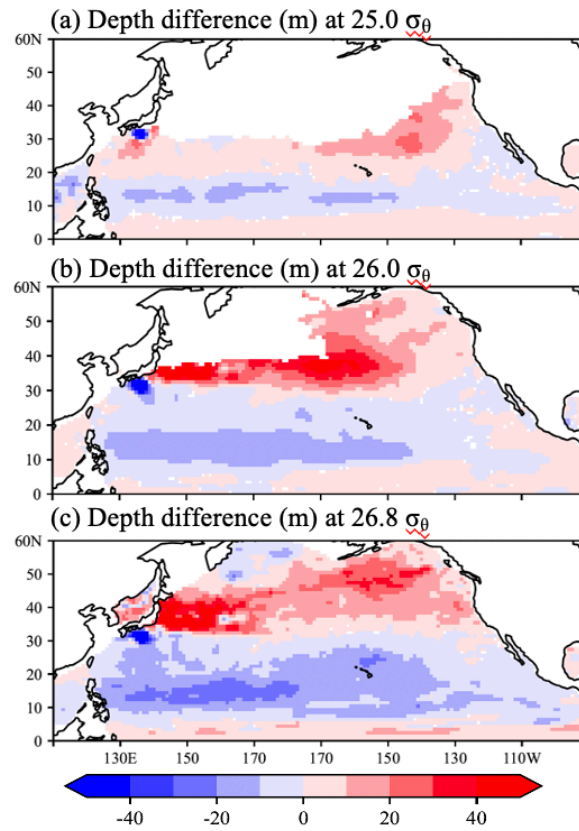


681

682 **Figure 7** Horizontal distributions of the changing rates ($\mu\text{mol/kg/yr}$) of each factor contributing to the
 683 rate of O_2 change on 25.0, 26.0, and 26.8 σ_{θ} in Eq. (1). The rate of O_2 change on each isopycnal
 684 surface is decomposed into the following components: (ii) the apparent contribution from vertical
 685 heave (deepening or shoaling) of isopycnal surfaces associated with warming and/or surface
 686 freshening; (iii) the contribution from changes in oxygen solubility (O_2^{sat}) associated with
 687 temperature and salinity variations; (iv) the contribution from vertical heave acting on the background
 688 solubility gradient; (v) the contribution from net changes in apparent oxygen utilization (AOU)
 689 associated with air–sea disequilibrium, biological activity, and lateral advection and/or circulation; and
 690 (vi) the contribution from vertical heave acting on AOU gradients, independent of solubility changes.
 691 This decomposition is applied to the reconstructed dissolved oxygen fields obtained from linear

692 regression analysis.

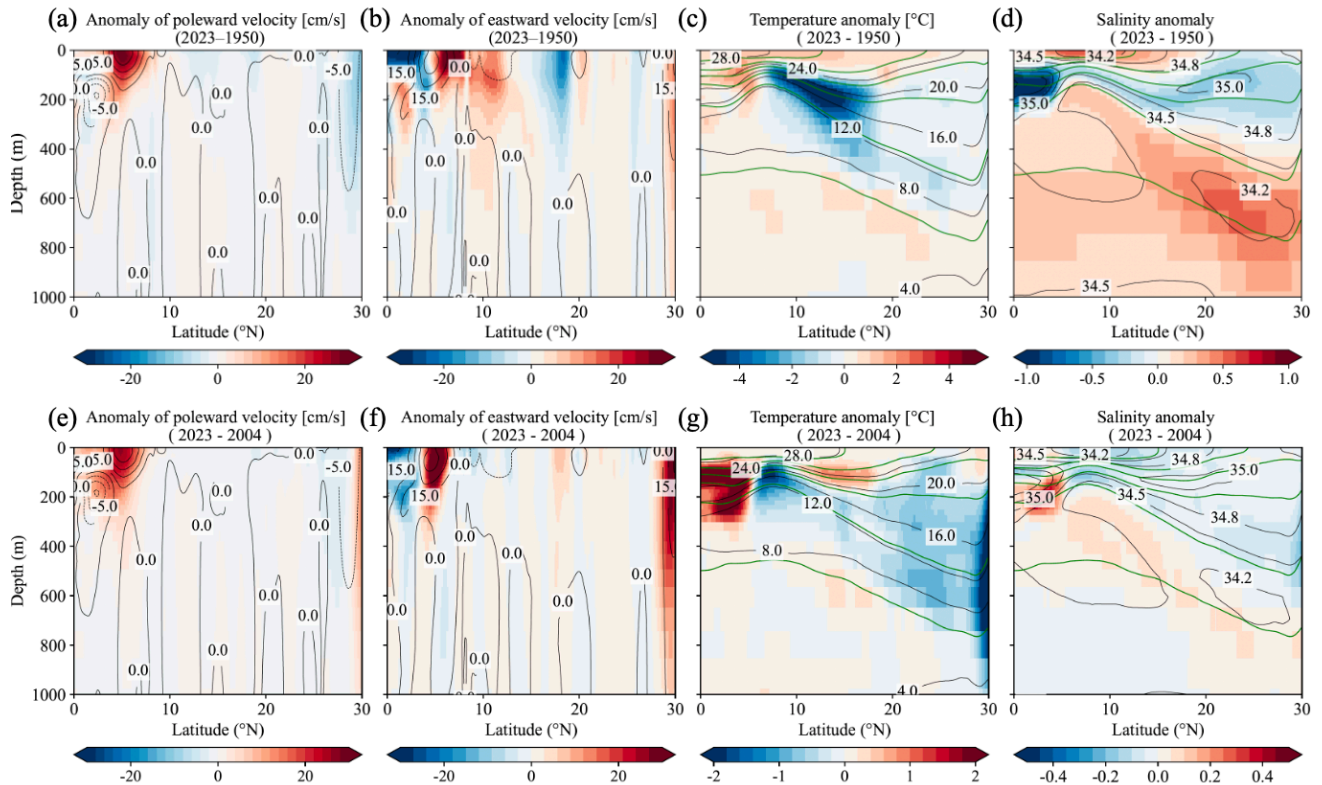
693



694

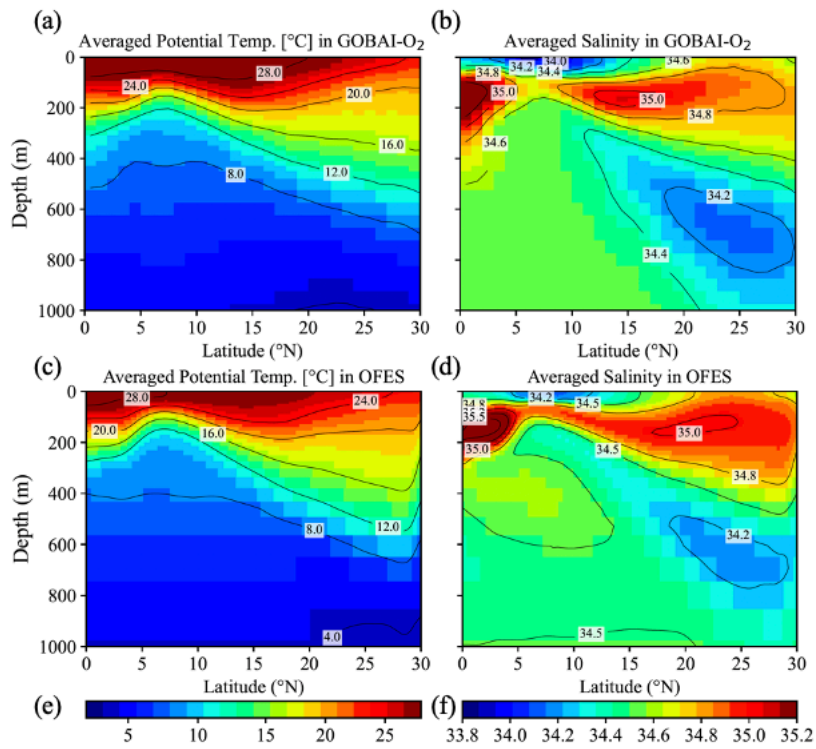
695 **Figure 8** Depth difference (m) between the 5-year averaged data in March, 2004–2009 and 2018–
696 2023 at 25.0, 26.0, and 26.8 σ_{θ} . The reconstructed O₂ data estimated from the linear regression analysis
697 were used in this calculation. Positive and negative values indicate the deepening and shallowing,
698 respectively, from the depth of each density in 2004–2023.

699



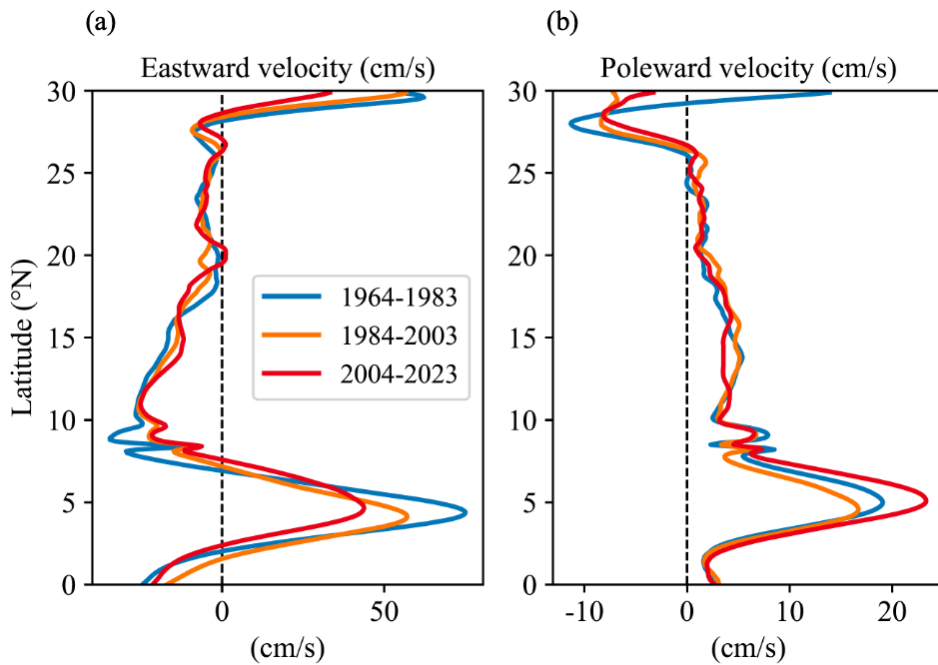
700

701 **Figure 9.** Anomaly of poleward and eastward velocity, potential temperature, and salinity in the OFES
 702 model outputs from 1950 to 2023 (a–d) and from 2004 to 2023 (e–h), respectively, in the 137°E line.
 703 Contours of averaged values of poleward and eastward velocity, potential temperature, and salinity
 704 during the target period are also shown in each figure. Green contour lines in (c–d, g–h) indicate the
 705 average potential density of 22, 23, 24, 25, 26, and 27 σ_{θ} , during the target periods.



706

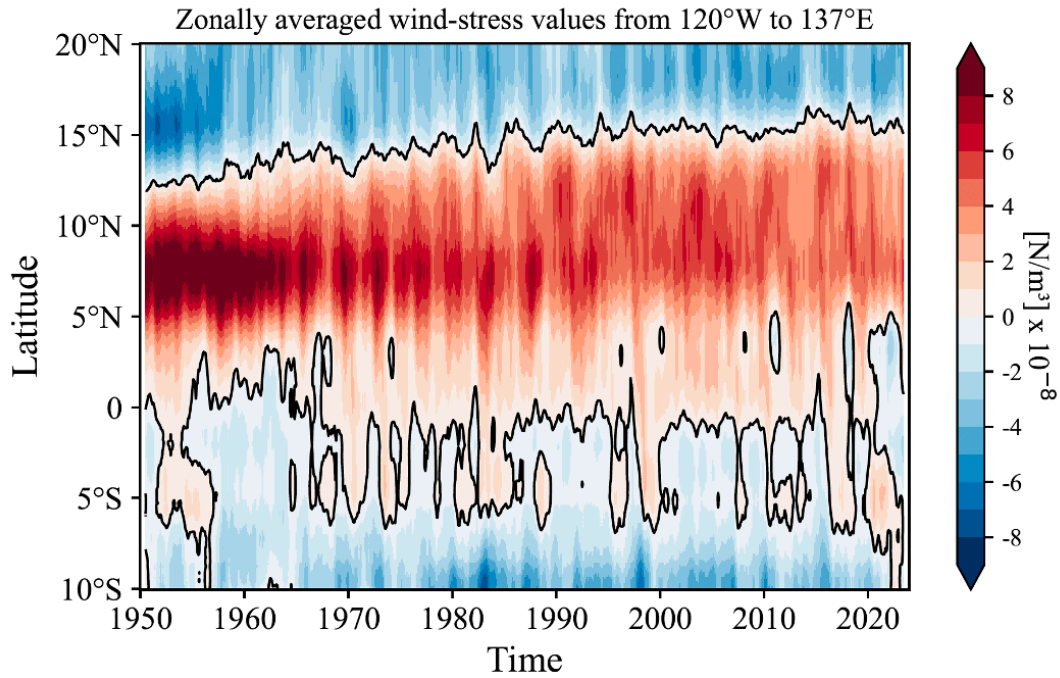
707 **Figure 10.** Averaged Potential Temperature (a, c) and salinity (b, d) in GOBAI-O₂ from 2004 to
 708 2023 and OFES data from 1950 to 2023, respectively, in the 137°E line.



709

710 **Figure 11.** Latitudinal distribution of averaged eastward (a) and poleward velocity (b) in the OFES
 711 data from 1964 to 1983, from 1984 to 2003, and from 2004 to 2023, respectively, in the 137°E line.

712



713

714 **Figure 12.** NCEP-NCAR wind-stress curl values zonally averaged from 137°E to 120° W from 1950
 715 to 2023. A 13-month running-mean filter has been applied in time.

716

717 **Appendix: Essential concepts and derivations for Equation (2–3)**

718 The essential concepts and derivations for equations (2) and (3) were originally proposed by Takatani
 719 et al. [2012] and subsequently described in detail by Sasano et al. [2015]. Here, we briefly summarize
 720 and follow their derivation.

721

722 When the temperature at a depth z_A increases from θ_A to θ_A' as a result of increased ocean heat
 723 content, the density at that depth decreases from σ_A to σ_A' . For simplicity, the vertical salinity profile
 724 is assumed to remain unchanged with time. As a consequence, the isopycnal surface of σ_A deepens
 725 from z_A to z_B (Figure S5). If surface freshening occurs simultaneously due to a net freshwater input,
 726 both the density decreases at z_A (from σ_A to σ_A') and the deepening of the isopycnal surface (from
 727 z_A to z_B) are enhanced. Because density is a function of temperature and salinity ($\sigma = f(\theta, S)$), the

728 density of the isopycnal surface σ_A can be expressed as

729
$$\sigma_A = f(\theta_A, S_A) \quad (\text{before warming}) \quad (\text{C1})$$

730
$$= f(\theta_B', S_B). \quad (\text{after warming}) \quad (\text{C2})$$

731 Here, S_A and S_B denote salinity at depth z_A and z_B , respectively, and θ_B' represents the temperature at
732 density σ_A at depth z_B after warming. The depth z_B is determined by satisfying Eqs. (C1) and (C2).
733 In the region where salinity decreases with depth (e.g., above the salinity minimum layer of NPIW),
734 $S_A > S_B$, and therefore $\theta_A > \theta_B'$. This implies that the potential temperature on an isopycnal surface
735 effectively decreases as a consequence of warming, and that biogeochemical properties on the same
736 isopycnal surface are also expected to change.

737

738 For a tracer X whose vertical profile with respect to depth does not change with time (e.g., salinity;
739 see Figure S5 (c)), the temporal change of X on the potential density surface σ_A is attributed solely
740 to the apparent change caused by the deepening of the isopycnal surface from z_A to z_B :

741
$$\frac{\partial X}{\partial t} = \left(\frac{\partial X}{\partial z} \cdot \frac{\partial z}{\partial t} \right) \quad (\text{C3})$$

742 Here, $\partial X/\partial t$ represents the temporal change of X observed on σ_A (gray arrows in Figure S5), z
743 denotes the depth of σ_A , $\partial X/\partial z$ is the vertical gradient of X with respect to the depth (assumed to be
744 time-invariant), and $\partial z/\partial t$ is the rate of deepening of the isopycnal surface σ_A . The product
745 $\partial X/\partial z \cdot \partial z/\partial t$ represents the effect of isopycnal deepening (white arrows in Figure S5),
746 corresponding to the difference between the filled square and filled circle.

747

748 For a variable Y whose vertical profile evolves with time while warming occurs simultaneously, the
749 temporal change of Y on the density surface σ_A can be expressed as the sum of two components: the
750 contribution due to the isopycnal deepening from z_A to z_B and the net temporal change of Y ,

751 $(\partial Y/\partial t)_{net}$ between the time before and after warming:

752
$$\frac{\partial Y}{\partial t} = \left(\frac{\partial Y}{\partial z} \cdot \frac{\partial z}{\partial t} \right) + \left(\frac{\partial Y}{\partial t} \right)_{net} \quad (C4)$$

753 To evaluate the net change $(\partial Y/\partial z)_{net}$ (illustrated by the blue arrows of a difference in symbols
754 between filled square and open square in Figure S5), it is necessary to evaluate the contribution of the
755 temporal change of Y due to the isopycnal deepening and to subtract it from the change of Y observed
756 at density σ_A . For instance, the change of O_2^{sat} in Figure S5 (f) is observed along the gray isopycnal
757 surface (large white arrow), whereas the net change (large blue and pink arrows) is obtained as the
758 difference between the observed change and the deepening effect.

759

760 The dissolved oxygen concentration O_2 can be expressed as:

761
$$O_2 = O_2^{sat} - AOU, \quad (C5)$$

762 where O_2^{sat} is the oxygen saturation concentration (a function of temperature and salinity), and AOU
763 is “apparent oxygen utilization”, representing the oxygen consumed by biological processes since
764 subduction. Near the surface, AOU is typically small, and its contributions can be neglected.

765

766 Following Eq. (C4), the temporal change of O_2 on a given isopycnal surface at a fixed station is:

767
$$\frac{\partial O_2}{\partial t} = \left(\frac{\partial O_2}{\partial z} \cdot \frac{\partial z}{\partial t} \right) + \left(\frac{\partial O_2}{\partial t} \right)_{net}. \quad (C6)$$

768 Similarly,

769
$$\frac{\partial O_2^{sat}}{\partial t} = \left(\frac{\partial O_2^{sat}}{\partial z} \cdot \frac{\partial z}{\partial t} \right) + \left(\frac{\partial O_2^{sat}}{\partial t} \right)_{net}, \quad (C7)$$

770 and

771
$$\frac{\partial AOU}{\partial t} = \left(\frac{\partial(AOU)}{\partial z} \cdot \frac{\partial z}{\partial t} \right) + \left(\frac{\partial(AOU)}{\partial t} \right)_{net}. \quad (C8)$$

772 The term net is directly related to warming, because depends on temperature and salinity. If AOU does
 773 not change with time, that is, if changes in O_2 arise solely from changes in, then $\partial(AOU)/\partial t$ follows
 774 Eq. (C3) and $= 0$. If AOU varies with time, however, $\partial(AOU)/\partial t$ follows Eq. (C4) and $\neq 0$, as
 775 illustrated by the dashed gray line in Figure S5 (g).

776

777 Because O_2 is defined by Eq. (C5), the net temporal change of O_2 on an isopycnal surface is

$$778 \quad \left(\frac{\partial O_2}{\partial t}\right)_{net} = \left(\frac{\partial O_2^{sat}}{\partial t}\right)_{net} - \left(\frac{\partial(AOU)}{\partial t}\right)_{net}. \quad (C9)$$

779 Combining Eqs. (C6) and (C9), the total temporal change of O_2 on an isopycnal surface can be
 780 written as

$$781 \quad \left(\frac{\partial O_2}{\partial t}\right) = \left(\frac{\partial O_2}{\partial z} \cdot \frac{\partial z}{\partial t}\right) + \left(\frac{\partial O_2^{sat}}{\partial t}\right)_{net} - \left(\frac{\partial(AOU)}{\partial t}\right)_{net}, \quad (C10)$$

782 which corresponds to Eq. (1) in the main text. Eq. (C10) corresponds to an arrow in Figure S5 (e),
 783 represented from left to right by the large gray arrow, white, blue, and pink arrows. The large blue
 784 arrow is identical to Figure S5 (f), while the large pink arrow corresponds to Figure S5(g), but with
 785 its direction reversed. Finally, substituting Eqs. (C7) and (C8) into (C10)

$$786 \quad \frac{\partial O_2}{\partial t} = \left(\frac{\partial O_2}{\partial z} \frac{\partial z}{\partial t}\right) + \left(\frac{\partial O_2^{sat}}{\partial t} - \frac{\partial O_2^{sat}}{\partial z} \frac{\partial z}{\partial t}\right) - \left(\frac{\partial(AOU)}{\partial t} - \frac{\partial(AOU)}{\partial z} \frac{\partial z}{\partial t}\right), \quad (C11)$$

$$787 \quad \text{(i) } \quad \text{(ii) } \quad \text{(iii) } \quad \text{(iv) } \quad \text{(v) } \quad \text{(vi)}$$

788 which corresponds to Eq. (2) in the main text. Note: The signs in terms (v) and (vi) in Eq. (3) are
 789 reversed relative to those in Eq. (C11) for convenience.

790

791 Table A1 The physical interpretation of each term in the oxygen tendency decomposition shown in Eq.
 792 (3) and Eq. (C11) is summarized.

Term	Mathematical form	Physical interpretation
(ii)	$(\partial O_2 / \partial z)(\partial z / \partial t)$	Vertical heave acting on the O ₂ gradient
(iii)	$\partial O_2^{sat} / \partial t$	Solubility effect due to temperature and salinity changes
(iv)	$-(\partial O_2^{sat} / \partial z)(\partial z / \partial t)$	Vertical heave acting on the solubility gradient
(v)	$\partial AOU / \partial t$	AOU changes related to air–sea disequilibrium, biological activity and lateral circulation
(vi)	$-(\partial AOU / \partial z)(\partial z / \partial t)$	Vertical heave of the AOU gradient

793

794

795 **References:**

- 796 Alkire, M. B., D'Asaro, E., Lee, C., Jane Perry, M., Gray, A., Cetinić, I., et al. (2012). Estimates of
797 net community production and export using high-resolution, Lagrangian measurements of O₂, NO₃⁻,
798 and POC through the evolution of a spring diatom bloom in the North Atlantic. *Deep Sea Research*
799 *Part I: Oceanographic Research Papers*, 64, 157–174. <https://doi.org/10.1016/j.dsr.2012.01.012>
- 800 Behringer, D. W., & Xue, Y. (2004). Evaluation of the global ocean data assimilation system at NCEP:
801 The Pacific Ocean. 8th Symposium on Integrated Observing and Assimilation Systems for Atmosphere,
802 Oceans, and Land Surface, AMS 84th Annual Meeting, Washington State Convention and Trade Center,
803 Seattle, Washington, 11-15. <https://ams.confex.com/ams/pdfpapers/70720.pdf>
- 804 Behringer, D. W. (2007). The Global Ocean Data Assimilation System (GODAS) at NCEP. 11th
805 Symp. on Integrated Observing and Assimilation Systems for Atmosphere, Oceans, and Land
806 Surface, San Antonio, TX, Amer. Meteor. Soc., 3.3. [Available online
807 at <https://ams.confex.com/ams/pdfpapers/119541.pdf>.]
- 808 Berman-Frank, I., Lundgren, P., & Falkowski, P. (2003). Nitrogen fixation and photosynthetic oxygen
809 evolution in cyanobacteria. *Research in Microbiology*, 154(3), 157–164.
810 [https://doi.org/10.1016/S0923-2508\(03\)00029-9](https://doi.org/10.1016/S0923-2508(03)00029-9)

811 Bittig, H. C., Fiedler, B., Scholz, R., Krahnemann, G., & Körtzinger, A. (2014). Time response of oxygen
812 optodes on profiling platforms and its dependence on flow speed and temperature. *Limnology and*
813 *Oceanography: Methods*, 12(8), 617–636. <https://doi.org/10.4319/lom.2014.12.617>

814 Bittig, H. C., & Körtzinger, A. (2015). Tackling Oxygen Optode Drift: Near-Surface and In-Air
815 Oxygen Optode Measurements on a Float Provide an Accurate in Situ Reference.
816 <https://doi.org/10.1175/JTECH-D-14-00162.1>

817 Bittig, H. C., Körtzinger, A., Neill, C., van Ooijen, E., Plant, J. N., Hahn, J., et al. (2018a). Oxygen
818 Optode Sensors: Principle, Characterization, Calibration, and Application in the Ocean. *Frontiers in*
819 *Marine Science*, 4. <https://doi.org/10.3389/fmars.2017.00429>

820 Bittig, H. C., Steinhoff, T., Claustre, H., Fiedler, B., Williams, N. L., Sauzède, R., et al. (2018b). An
821 Alternative to Static Climatologies: Robust Estimation of Open Ocean CO₂ Variables and Nutrient
822 Concentrations From T, S, and O₂ Data Using Bayesian Neural Networks. *Frontiers in Marine Science*,
823 5. <https://doi.org/10.3389/fmars.2018.00328>

824 Bopp, L., Resplandy, L., Orr, J. C., Doney, S. C., Dunne, J. P., Gehlen, M., et al. (2013). Multiple
825 stressors of ocean ecosystems in the 21st century: projections with CMIP5 models. *Biogeosciences*,
826 10(10), 6225–6245. <https://doi.org/10.5194/bg-10-6225-2013>

827 Boyer, T. P., and S. Levitus (1997), Objective Analyses of Temperature and Salinity for the World
828 Ocean on a 1/48 Grid, vol. 11, NOAA Atlas NESDIS, Natl. Oceanic and Atmos. Admin., Silver Spring,
829 Md.

830 Boyer, T. P., Antonov, J. I., Baranova, O. K., Coleman, C., Garcia, H. E., Grodsky, A., et al. (2013).
831 World Ocean Database 2013. Retrieved from
832 <https://repository.oceanbestpractices.org/handle/11329/357>

833 Breiman, L. (2001). Random Forests. *Machine Learning*, 45(1), 5–32.
834 <https://doi.org/10.1023/A:1010933404324>

835 Breitburg, D., Levin, L. A., Oschlies, A., Grégoire, M., Chavez, F. P., Conley, D. J., et al. (2018).
836 Declining oxygen in the global ocean and coastal waters. *Science*, 359(6371), eaam7240.
837 <https://doi.org/10.1126/science.aam7240>

838 Bushinsky, S. M., Emerson, S. R., Riser, S. C., & Swift, D. D. (2016). Accurate oxygen measurements
839 on modified Argo floats using in situ air calibrations. *Limnology and Oceanography: Methods*, 14(8),
840 491–505. <https://doi.org/10.1002/lom3.10107>

841 Bushinsky, S.M., Nachod, Z., Fassbender, A.J., Tamsitt, V., Takeshita, Y., Williams, N., 2025. Offset
842 Between Profiling Float and Shipboard Oxygen Observations at Depth Imparts Bias on Float pH and
843 Derived pCO₂. *Global Biogeochemical Cycles* 39, e2024GB008185.
844 <https://doi.org/10.1029/2024GB008185>

845 Chen, X., Qiu, B., Du, Y., Chen, S., & Qi, Y. (2016). Interannual and interdecadal variability of the
846 North Equatorial Countercurrent in the Western Pacific. *Journal of Geophysical Research: Oceans*,
847 121(10), 7743–7758. <https://doi.org/10.1002/2016JC012190>

848 Claustre, H., Johnson, K. S., & Takeshita, Y. (2020). Observing the Global Ocean with
849 Biogeochemical-Argo. *Annual Review of Marine Science*, 12(Volume 12, 2020), 23–48.
850 <https://doi.org/10.1146/annurev-marine-010419-010956>

851 D’Asaro, E. A., & McNeil, C. (2013). Calibration and Stability of Oxygen Sensors on Autonomous
852 Floats. <https://doi.org/10.1175/JTECH-D-12-00222.1>

853 Drucker, R., & Riser, S. C. (2016). In situ phase-domain calibration of oxygen Optodes on profiling
854 floats. *Methods in Oceanography*, 17, 296–318. <https://doi.org/10.1016/j.mio.2016.09.007>

855 Estapa, M. L., Feen, M. L., & Breves, E. (2019). Direct Observations of Biological Carbon Export
856 From Profiling Floats in the Subtropical North Atlantic. *Global Biogeochemical Cycles*, 33(3), 282–
857 300. <https://doi.org/10.1029/2018GB006098>

858 Giglio, D., Lyubchich, V., & Mazloff, M. R. (2018). Estimating Oxygen in the Southern Ocean Using
859 Argo Temperature and Salinity. *Journal of Geophysical Research: Oceans*, 123(6), 4280–4297.
860 <https://doi.org/10.1029/2017JC013404>

861 Helm, K. P., Bindoff, N. L., & Church, J. A. (2011). Observed decreases in oxygen content of the
862 global ocean. *Geophysical Research Letters*, 38(23). <https://doi.org/10.1029/2011GL049513>

863 Ito, T., Minobe, S., Long, M. C., & Deutsch, C. (2017). Upper ocean O₂ trends: 1958–2015.
864 *Geophysical Research Letters*, 44(9), 4214–4223. <https://doi.org/10.1002/2017GL073613>

865 Ito, T., Cervania, A., Cross, K., Ainchwar, S., & Delawalla, S. (2024). Mapping Dissolved Oxygen
866 Concentrations by Combining Shipboard and Argo Observations Using Machine Learning Algorithms.
867 *Journal of Geophysical Research: Machine Learning and Computation*, 1(3), e2024JH000272.
868 <https://doi.org/10.1029/2024JH000272>

869 Johnson, K. S., Plant, J. N., Riser, S. C., & Gilbert, D. (2015). Air Oxygen Calibration of Oxygen
870 Optodes on a Profiling Float Array. <https://doi.org/10.1175/JTECH-D-15-0101.1>

871 Johnson, K. S., Plant, J. N., Coletti, L. J., Jannasch, H. W., Sakamoto, C. M., Riser, S. C., et al. (2017).
872 Biogeochemical sensor performance in the SOCCOM profiling float array. *Journal of Geophysical*
873 *Research: Oceans*, 122(8), 6416–6436. <https://doi.org/10.1002/2017JC012838>

874 Johnson, K. S., & Bif, M. B. (2021). Constraint on net primary productivity of the global ocean by
875 Argo oxygen measurements. *Nature Geoscience*, 14(10), 769–774. [https://doi.org/10.1038/s41561-](https://doi.org/10.1038/s41561-021-00807-z)
876 [021-00807-z](https://doi.org/10.1038/s41561-021-00807-z)

877 Kalnay, E., Kanamitsu, M., Kistler, R., Collins, W., Deaven, D., Gandin, L., et al. (1996). The
878 NCEP/NCAR 40-Year Reanalysis Project. Retrieved from
879 [https://journals.ametsoc.org/view/journals/bams/77/3/1520-](https://journals.ametsoc.org/view/journals/bams/77/3/1520-0477_1996_077_0437_tnyrp_2_0_co_2.xml)
880 [0477_1996_077_0437_tnyrp_2_0_co_2.xml](https://journals.ametsoc.org/view/journals/bams/77/3/1520-0477_1996_077_0437_tnyrp_2_0_co_2.xml)

881 Kara, A. B., Rochford, P. A., & Hurlburt, H. E. (2000). An optimal definition for ocean mixed layer
882 depth. *Journal of Geophysical Research: Oceans*, *105*(C7), 16803–16821.
883 <https://doi.org/10.1029/2000JC900072>

884 Keeling, R. F., Körtzinger, A., & Gruber, N. (2010). Ocean Deoxygenation in a Warming World.
885 *Annual Review of Marine Science*, *2* (Volume 2, 2010), 199–229.
886 <https://doi.org/10.1146/annurev.marine.010908.163855>

887 Kolodziejczyk, N., Portela, E., Thierry, V., & Prigent, A. (2024). ISASO2: recent trends and regional
888 patterns of ocean dissolved oxygen change. *Earth System Science Data*, *16*(11), 5191–5206.
889 <https://doi.org/10.5194/essd-16-5191-2024>

890 Körtzinger, A., Schimanski, J., & Send, U. (2005). High Quality Oxygen Measurements from Profiling
891 Floats: A Promising New Technique. <https://doi.org/10.1175/JTECH1701.1>

892 Kwiatkowski, L., Torres, O., Bopp, L., Aumont, O., Chamberlain, M., Christian, J. R., et al. (2020).
893 Twenty-first century ocean warming, acidification, deoxygenation, and upper-ocean nutrient and
894 primary production decline from CMIP6 model projections. *Biogeosciences*, *17*(13), 3439–3470.
895 <https://doi.org/10.5194/bg-17-3439-2020>

896 Lauvset, S. K., Lange, N., Tanhua, T., Bittig, H. C., Olsen, A., Kozyr, A., et al. (2022b).
897 GLODAPv2.2022: the latest version of the global interior ocean biogeochemical data product. *Earth*
898 *System Science Data*, *14*(12), 5543–5572. <https://doi.org/10.5194/essd-14-5543-2022>

899 Li, C., Huang, Jianping, Ding, L., Liu, X., Yu, H., Huang, Jiping, 2020. Increasing Escape of Oxygen
900 From Oceans Under Climate Change. *Geophysical Research Letters* *47*, e2019GL086345.
901 <https://doi.org/10.1029/2019GL086345>

902 Limburg, K. E., Breitburg, D., Swaney, D. P., & Jacinto, G. (2020). Ocean Deoxygenation: A Primer.
903 *One Earth*, *2*(1), 24–29. <https://doi.org/10.1016/j.oneear.2020.01.001>

904 Masumoto, Y., Sasaki, H., Kagimoto, T., Komori, N., Ishida, A., Sasai, Y., et al. (2004). A fifty-year
905 eddy-resolving simulation of the world ocean: Preliminary outcomes of OFES (OGCM for the Earth

906 Simulator). *Journal of the Earth Simulator*, 1,35–56. [https://www.jamstec.](https://www.jamstec.go.jp/ceist/j/publication/journal/jes_vol.1/pdf/JES1-3.2-masumoto.pdf)
907 [go.jp/ceist/j/publication/journal/jes_vol.1/pdf/JES1-3.2-masumoto.pdf](https://www.jamstec.go.jp/ceist/j/publication/journal/jes_vol.1/pdf/JES1-3.2-masumoto.pdf)

908 Masumoto, Y. (2010). Sharing the results of a high-resolution ocean general circulation model under
909 a multi-discipline framework—a review of OFES activities. *Ocean Dynamics*, 60(3), 633–652.
910 <https://doi.org/10.1007/s10236-010-0297-z>

911 Maurer, T. L., Plant, J. N., & Johnson, K. S. (2021). Delayed-Mode Quality Control of Oxygen, Nitrate,
912 and pH Data on SOCCOM Biogeochemical Profiling Floats. *Frontiers in Marine Science*, 8.
913 <https://doi.org/10.3389/fmars.2021.683207>

914 Nakamura, T., & Awaji, T. (2004). Tidally induced diapycnal mixing in the Kuril Straits and its role
915 in water transformation and transport: A three-dimensional nonhydrostatic model experiment. *Journal*
916 *of Geophysical Research: Oceans*, 109(C9). <https://doi.org/10.1029/2003JC001850>

917 Nakamura, T., Awaji, T., Hatayama, T., Akitomo, K., Takizawa, T., Kono, T., et al. (2000a). The
918 Generation of Large-Amplitude Unsteady Lee Waves by Subinertial K1 Tidal Flow: A Possible
919 Vertical Mixing Mechanism in the Kuril Straits. Retrieved from
920 [https://journals.ametsoc.org/view/journals/phoc/30/7/1520-](https://journals.ametsoc.org/view/journals/phoc/30/7/1520-0485_2000_030_1601_tgolau_2.0.co_2.xml)
921 [0485_2000_030_1601_tgolau_2.0.co_2.xml](https://journals.ametsoc.org/view/journals/phoc/30/7/1520-0485_2000_030_1601_tgolau_2.0.co_2.xml)

922 Nakamura, T., Awaji, T., Hatayama, T., Akitomo, K., & Takizawa, T. (2000b). Tidal Exchange
923 through the Kuril Straits. Retrieved from [https://journals.ametsoc.org/view/journals/phoc/30/7/1520-](https://journals.ametsoc.org/view/journals/phoc/30/7/1520-0485_2000_030_1622_tetts_2.0.co_2.xml)
924 [0485_2000_030_1622_tetts_2.0.co_2.xml](https://journals.ametsoc.org/view/journals/phoc/30/7/1520-0485_2000_030_1622_tetts_2.0.co_2.xml)

925 Nicholson, D. P., & Feen, M. L. (2017). Air calibration of an oxygen optode on an underwater glider.
926 *Limnology and Oceanography: Methods*, 15(5), 495–502. <https://doi.org/10.1002/lom3.10177>

927 Ogata, T., & Nonaka, M. (2020). Mechanisms of Long-Term Variability and Recent Trend of Salinity
928 Along 137°E. *Journal of Geophysical Research: Oceans*, 125(2), e2019JC015290.
929 <https://doi.org/10.1029/2019JC015290>

930 Pacanowski, R. C., and S. M. Griffies (2000), MOM 3.0 Manual, Technical Report 4, 680 pp., Geophys.
931 Fluid Dyn. Lab., Princeton, N. J. Philander, S. G. H. (1990), El Niño, La Niña, and the Southern
932 Oscillation, pp. 293, Academic Press, San Diego, Calif.

933 Pörtner, H. O., & Farrell, A. P. (2008). Physiology and Climate Change. *Science*, 322(5902), 690–692.
934 <https://doi.org/10.1126/science.1163156>

935 Pozo Buil, M., & Di Lorenzo, E. (2017). Decadal dynamics and predictability of oxygen and
936 subsurface tracers in the California Current System. *Geophysical Research Letters*, 44(9), 4204–4213.
937 <https://doi.org/10.1002/2017GL072931>

938 Reid, J. L. (1997). On the total geostrophic circulation of the Pacific Ocean: flow patterns, tracers, and
939 transports. *Progress in Oceanography*, 39(4), 263–352. [https://doi.org/10.1016/S0079-](https://doi.org/10.1016/S0079-6611(97)00012-8)
940 [6611\(97\)00012-8](https://doi.org/10.1016/S0079-6611(97)00012-8)

941 Roemmich, D., & Gilson, J. (2009). The 2004–2008 mean and annual cycle of temperature, salinity,
942 and steric height in the global ocean from the Argo Program. *Progress in Oceanography*, 82(2), 81–
943 100. <https://doi.org/10.1016/j.pocean.2009.03.004>

944 Sampaio, E., Santos, C., Rosa, I. C., Ferreira, V., Pörtner, H.-O., Duarte, C. M., et al. (2021). Impacts
945 of hypoxic events surpass those of future ocean warming and acidification. *Nature Ecology &*
946 *Evolution*, 5(3), 311–321. <https://doi.org/10.1038/s41559-020-01370-3>

947 Sasaki, H., Nonaka, M., Masumoto, Y., Sasai, Y., Uehara, H., & Sakuma, H. (2008). An Eddy-
948 Resolving Hindcast Simulation of the Quasiglobal Ocean from 1950 to 2003 on the Earth Simulator.
949 In K. Hamilton & W. Ohfuchi (Eds.), *High Resolution Numerical Modelling of the Atmosphere and*
950 *Ocean* (pp. 157–185). New York, NY: Springer. https://doi.org/10.1007/978-0-387-49791-4_10

951 Sasano, D., Takatani, Y., Kosugi, N., Nakano, T., Midorikawa, T., & Ishii, M. (2015). Multidecadal
952 trends of oxygen and their controlling factors in the western North Pacific. *Global Biogeochemical*
953 *Cycles*, 29(7), 935–956. <https://doi.org/10.1002/2014GB005065>

954 Sasano, D., Takatani, Y., Kosugi, N., Nakano, T., Midorikawa, T., & Ishii, M. (2018). Decline and
955 Bidecadal Oscillations of Dissolved Oxygen in the Oyashio Region and Their Propagation to the
956 Western North Pacific. *Global Biogeochemical Cycles*, 32(6), 909–931.
957 <https://doi.org/10.1029/2017GB005876>

958 Schmidtko, S., Stramma, L., & Visbeck, M. (2017). Decline in global oceanic oxygen content during
959 the past five decades. *Nature*, 542(7641), 335–339. <https://doi.org/10.1038/nature21399>

960 Sharp, J. D., Fassbender, A. J., Carter, B. R., Johnson, G. C., Schultz, C., Dunne, J. P. (2022). GOBAI-
961 O₂: A Global Gridded Monthly Dataset of Ocean Interior Dissolved Oxygen Concentrations Based on
962 Shipboard and Autonomous Observations (NCEI Accession 0259304). NOAA National Centers for
963 Environmental Information. Dataset. <https://doi.org/10.25921/z72m-yz67>.

964 Sharp, J. D., Fassbender, A. J., Carter, B. R., Johnson, G. C., Schultz, C., & Dunne, J. P. (2023).
965 GOBAI-O₂: temporally and spatially resolved fields of ocean interior dissolved oxygen over nearly 2
966 decades. *Earth System Science Data*, 15(10), 4481–4518. <https://doi.org/10.5194/essd-15-4481-2023>

967 Stramma, L., Johnson, G. C., Sprintall, J., & Mohrholz, V. (2008). Expanding Oxygen-Minimum
968 Zones in the Tropical Oceans. *Science*, 320(5876), 655–658. <https://doi.org/10.1126/science.1153847>

969 Stramma, L., Schmidtko, S., Bograd, S. J., Ono, T., Ross, T., Sasano, D., & Whitney, F. A. (2020).
970 Trends and decadal oscillations of oxygen and nutrients at 50 to 300 m depth in the equatorial
971 and North Pacific. *Biogeosciences*, 17(3), 813–831. <https://doi.org/10.5194/bg-17-813-2020>

972 Stramma, L., & Schmidtko, S. (2021). Tropical deoxygenation sites revisited to investigate oxygen
973 and nutrient trends. *Ocean Science*, 17(3), 833–847. <https://doi.org/10.5194/os-17-833-2021>

974 Suga, T., Takei, Y., & Hanawa, K. (1997). Thermostad Distribution in the North Pacific Subtropical
975 Gyre: The Central Mode Water and the Subtropical Mode Water. Retrieved from
976 [https://journals.ametsoc.org/view/journals/phoc/27/1/1520-](https://journals.ametsoc.org/view/journals/phoc/27/1/1520-0485_1997_027_0140_tditnp_2.0.co_2.xml)
977 [0485_1997_027_0140_tditnp_2.0.co_2.xml](https://journals.ametsoc.org/view/journals/phoc/27/1/1520-0485_1997_027_0140_tditnp_2.0.co_2.xml)

978 Suga, T., Motoki, K., Aoki, Y., & Macdonald, A. M. (2004). The North Pacific Climatology of Winter
979 Mixed Layer and Mode Waters. Retrieved from
980 [https://journals.ametsoc.org/view/journals/phoc/34/1/1520-
981 0485_2004_034_0003_tnpcow_2.0.co_2.xml](https://journals.ametsoc.org/view/journals/phoc/34/1/1520-0485_2004_034_0003_tnpcow_2.0.co_2.xml)

982 Takatani, Y., Sasano, D., Nakano, T., Midorikawa, T., & Ishii, M. (2012). Decrease of dissolved
983 oxygen after the mid-1980s in the western North Pacific subtropical gyre along the 137°E repeat
984 section. *Global Biogeochemical Cycles*, 26(2). <https://doi.org/10.1029/2011GB004227>

985 Takeshita, Y., Martz, T. R., Johnson, K. S., Plant, J. N., Gilbert, D., Riser, S. C., et al. (2013). A
986 climatology-based quality control procedure for profiling float oxygen data. *Journal of Geophysical
987 Research: Oceans*, 118(10), 5640–5650. <https://doi.org/10.1002/jgrc.20399>

988 Udaya Bhaskar, T. V. S., Sarma, V. V. S. S., & Pavan Kumar, J. (2021). Potential Mechanisms
989 Responsible for Spatial Variability in Intensity and Thickness of Oxygen Minimum Zone in the Bay
990 of Bengal. *Journal of Geophysical Research: Biogeosciences*, 126(6), e2021JG006341.
991 <https://doi.org/10.1029/2021JG006341>

992 Winkler, L. W. (1888). Die Bestimmung des im Wasser gelösten Sauerstoffes. *Berichte Der Deutschen
993 Chemischen Gesellschaft*, 21(2), 2843–2854. <https://doi.org/10.1002/cber.188802102122>

994 Wolf, M. K., Hamme, R. C., Gilbert, D., Yashayaev, I., & Thierry, V. (2018). Oxygen Saturation
995 Surrounding Deep Water Formation Events in the Labrador Sea From Argo-O₂ Data. *Global
996 Biogeochemical Cycles*, 32(4), 635–653. <https://doi.org/10.1002/2017GB005829>

997 Xu, L., Wang, K., & Wu, B. (2022). Weakening and Poleward Shifting of the North Pacific Subtropical
998 Fronts from 1980 to 2018. *Journal of Physical Oceanography*, 52(3), 399-417.
999 <https://doi.org/https://doi.org/10.1175/JPO-D-21-0170.1>

1000 Yang, H., Lohmann, G., Krebs-Kanzow, U., Ionita, M., Shi, X., Sidorenko, D., et al. (2020). Poleward
1001 Shift of the Major Ocean Gyres Detected in a Warming Climate. *Geophysical Research Letters*, 47(5),
1002 e2019GL085868. <https://doi.org/10.1029/2019GL085868>

1003 Yasuda, I. (2004). North Pacific Intermediate Water: Progress in SAGE (SubArctic Gyre Experiment)
1004 and Related Projects. *Journal of Oceanography*, 60(2), 385–395.
1005 <https://doi.org/10.1023/B:JOCE.0000038344.25081.42>

1006 You, Y. (2003). The pathway and circulation of North Pacific Intermediate Water. *Geophysical*
1007 *Research Letters*, 30(24). <https://doi.org/10.1029/2003GL018561>

1008

1009

1010